UNIVERSITY OF ÇUKUROVA
INSTITUTE OF NATURAL AND APPLIED SCIENCES

MSc. THESIS

Dilber UZUN

2008 BEAM TEST OF CMS-CASTOR PROTOTYPE IV AND 2008-2009 CMS-HF TEST OF ONLINE RADIATION DAMAGE MONITORING SYSTEM

DEPARTMENT OF PHYSICS

ADANA, 2010

INSTUTUTE OF NATURAL AND APPLIED SCIENCE

UNIVERSITY OF ÇUKUROVA

2008 BEAM TEST OF CMS-CASTOR PROTOTYPE IV AND CMS-HF TEST OF ONLINE RADIATION DAMAGE MONITORING SYSTEM

By Dilber UZUN

A THESIS OF MASTER OF SCIENCE
DEPARTMENT OF PHYSICS

We certify that the thesis titled above was reviewed and approved for the award of degree of Master of Science by board of jury on 14/01/ 2010.

Signature	Signature	Signature
Assoc.Prof.Dr.İsa DUMANOĞLU	**Prof.DrGülsen ÖNENGÜT**	**Assoc.Prof.Dr. Mehmet TEKDAL**
SUPERVISOR	**MEMBER**	**MEMBER**

This MSc Thesis is performed in the Physics Department of the Institute of Natural and Applied Science of Çukurova University.
Registration Number:

Prof. Dr. İlhami YEĞİNGİL
Director
The Institute of Natural and Applied Science

This study was supported by Çukurova University's Scientific Research Fund.
Project Number: FEF.2008.YL.5

ÇUKUROVA ÜNİVERSİTESİ
FEN BİLİMLERİ ENSTİTÜSÜ

2008 CMS-CASTOR KALORİMETRESİNİN DÖRDÜNCÜ PROTOTİP HÜZME TESTİ ANALİZİ VE CMS-HF KALORİMETRESİNDEKİ HF FİBERLERİNİN RADDAM SİSTEMİ İLE MONİTÖRÜ

Dilber UZUN

MASTER TEZİ
FİZİK ANABİLİM DALI

Bu tez 14/01/2010 tarihinde aşağıdaki jüri üyeleri tarafından oybirliği/oyçokluğu ile kabul edilmiştir.

İmza	İmza	İmza
Doç.Dr. İsa DUMANOĞLU	**Prof.Dr. Gülsen ÖNENGÜT**	**Yrd.Doç.Dr. Mehmet TEKDAL**
DANIŞMAN	**ÜYE**	**ÜYE**

Bu tez Enstitümüz Fizik Anabilim Dalında hazırlanmıştır.

Kod No:

Prof. Dr. İlhami YEĞİNGİL
Enstitü Müdürü
İmza ve Mühür

Not: Bu tezde kullanılan özgün ve başka kaynaktan yapılan bildirişlerin, çizelge, şekil ve fotoğrafların kaynak gösterilmeden kullanımı, 5846 sayılı Fikir ve Sanat Eserleri Kanunundaki hükümlere tabidir.

ABSTRACT

MSc THESIS

2008 BEAM TEST OF CMS-CASTOR PROTOTYPE IV AND CMS-HF TEST OF ONLINE RADIATION DAMAGE MONITORING SYSTEM

Dilber UZUN

DEPARTMENT OF PHYSICS
INSTITUTE OF NATURAL AND APPLIED SCIENCES
UNIVERSITY OF ÇUKUROVA

Supervisor : Assoc. Prof. Dr. İsa DUMANOĞLU
Year : 2010, Pages: 66
Jury : Assoc. Prof. Dr. İsa DUMANOĞLU
Prof. Dr. Gülsen ÖNENGÜT
Assist. Prof. Dr. Mehmet TEKDAL

CASTOR is a sampling electromagnetic/hadronic calorimeter, to be installed as a sub- detector of the CMS Experiment at the LHC. It is positioned in the very forward region, 14.38 m away from the interaction point and covering the pseudo rapidity range $5.15 < h < 6.6$. In order to test the final design of the CASTOR calorimeter, last prototype of the CASTOR was tested at CERN/SPS H2 beam line in 2008. The energy linearity and resolution as well as the spatial resolution of the prototype for the electromagnetic and hadronic showers were studied with electrons, pions and muons during the test beam. In this thesis, energy scan was studied using $E = 10,20,50,120,150,200$ GeV electrons. Also Radiation Damage Monitoring (Raddam) system of HF calorimeter was studied using data which was taken in 2008-2009.

Key Words: LHC, CMS, CASTOR, HF, Raddam

ÖZ

YÜKSEK LİSANS

2008 CMS-CASTOR KALORİMETRESİNİN DÖRDÜNCÜ PROTOTİP HÜZME TESTİ ANALİZİ VE CMS-HF KALORİMETRESİNDEKİ HF FİBERLERİNİNRADDAM SİSTEMİ İLE MONİTÖRÜ

Dilber UZUN

ÇUKUROVA ÜNİVERSİTESİ
FEN BİLİMLERİ ENSTİTÜSÜ
FİZİK ANABİLİM DALI

Danışman : Doç. Dr. İsa DUMANOĞLU
Yıl : 2010, Sayfa: 66
Jüri : Doç Dr. İsa DUMANOĞLU
Prof. Dr. Gülsen ÖNENGÜT
Yrd. Doç. Dr. Mehmet TEKDAL

CMS deneyinin bir alt dedektorü olan CASTOR, elektromanyetik ve hadronik bölümlere sahip bir örnekleme kalorimetresidir. Etkileşme noktasından 14,38 m uzağa yerleştirilecek olan CASTOR'un pseudorapidite bölgesi $5.15 < h < 6.6$ aralığını kapsamaktadır. CASTOR kalorimetresi için en son dizayn edilen prototip IV, kuvartz ve tungsten plakalardan oluşup testleri CERN/SPS H2 hüzme test alanında 2008 yılında yapılmıştır.Bu prototip farklı enerjilerdeki müon, pion ve elektronlarla test edilmiştir. Bu çalışmada bu prototipin, $E = 10,20,50,120,150,200$ GeV enerjilere sahip elektronlar kullanılarak, kalorimetrenin çözünürlüğü ve doğrusallığı araştırılmıştır. Bu çalışmalara ek olarak, HF kalorimetresinde, 2008-2009 yılında alınan verileri kullanarak HF kalorimetresindeki fiberlerin. radyasyon hasar belirleme sistemi üzerine yapılan analiz sonuçları sunulmuştur.

Anahtar Kelimeler: BHÇ, CMS, CASTOR, HF, Raddam.

ACKNOWLEDGEMENT

First of all, I wish to thank and express my gratitude towards my supervisor, Assoc. Prof. Dr. İsa Dumanoğlu, for his encouragement and guidance throughout my education, including bachelor and this master study. It is a great chance for me to study with him and to have him as an advisor.

I would like to thank Panagiotis Katsas for his valuable suggestions and help during my research when I was at CERN. I am so pleased to work with him. Additionally, I am very grateful to met Kerem Cankoçak and Jean Pierre Merlo. They showed me the way how to deal with some specific problems that I was suffering from. I am always very pleased to discuss with them about physics.

I wish to thank all members of CASTOR collaboration for their valuable discussions and help, in particular, Kerstin Borras and Apostolos Panagiotou. I would like to thank all members of High Energy Physics group of Çukurova University for their help and support especially to Prof.Dr. Gülsen Önengüt.

I would like to express my deep gratitude and love to my family especially my beloved father, Mehmet UZUN, without his help I could not have done anything.

Finally, I would like to thank TAEK (Turkey Atomic Energy Authority) for their support during the time I have spent at CERN.

TABLE OF CONTENTS **PAGE**

LIST OF TABLES **PAGE**

LIST OF FIGURES **PAGE**

LIST OF SYMBOLS AND ABBREVIATIONS

SM : Standard Model

SUSY : Supersymmetry

BSM : Beyond Standard Model

LHC : Large Hadron Collider

CMS : Compact Muon Solenoid

CASTOR : Centauro and Strange Object Research Detector

ATLAS : A Torodial LHC Apparatus

ALICE : A Large Ion Collider Experiment

LHC : A Large Hadron Collider Beauty

CERN : European Nuclear Research Laboratory

RADDAM : Radiation Damage Monitoring

QCD : Quantum Chromo Dynamics

QGP : Quark Gluon Plasma

SQM : Strange Quark Matter

QM : Quark Matter

EM : Electromagnetic Channel

HAD : Hadronic Channel

SU : Sampling Unit

RU : Readout Unit

MeV : Million Electron Volts

GeV : Giga Electron Volts

TeV : Tera Electron Volts

PS : Proton Synchrotron

SPS **:** Super Proton Synchrotron

$\boldsymbol{P_T}$ **:** Transverse Momentum

$\boldsymbol{E_T}$ **:** Transverse Energy

Λ **:** Interaction Length

$\boldsymbol{X_0}$ **:** Radiation Length

A **:** Atomic Number

WC **:** Wire chamber

1. INTRODUCTION

Particle physics is a branch of physics that studies the elementary constituents of matter and radiation, and the interactions between them. It is also called high energy physics, because many elementary particles do not occur under normal circumstances in nature, but can be created and detected during energetic collisions of other particles, as is done in particle accelerators. Research in this area has produced a long list of particles. This is a list of different types of particles found or believed to exist in the whole of the universe. For individual lists of the different particles, see the individual pages given below. Elementary particles are particles with no measurable internal structure; that is, they are not composed of other particles. They are the fundamental objects of quantum field theory. Many families and sub-families of elementary particles exist. Elementary particles are classified according to their spin. Fermions have half-integer spin while bosons have integer spin. All the particles of the Standard Model have been observed, with the exception of the Higgs boson. (CMS Physics TDR, 2006)

1.1. The Standard Model

The current state of the classification of elementary particles is the Standard Model. The Standard Model of particle physics is a theory of three of the four known fundamental interactions and the elementary particles that take part in these interactions. These particles make up all visible matter in the universe. Every high energy physics experiment carried out since the mid-20th century has eventually yielded findings consistent with the Standard Model. Still, the Standard Model falls short of being a complete theory of fundamental interactions because it does not include gravitation, dark matter, or dark energy. It is not quite a complete description of leptons either, because it does not describe nonzero neutrino masses, although simple natural extensions do. The four known fundamental interaction are electromagnetism, strong interaction, weak interaction and gravitation. (CMS Physics TDR, 2006)

1.1.1. Fundamental Forces and Interactions

1.1.1.1. Electromagnetic Interaction

Electromagnetism is the physics of the electromagnetic field, a field that exerts a force on particles with the property of electric charge and is reciprocally affected by the presence and motion of such particles. A changing magnetic field produces an electric field. Similarly, a changing electric field generates a magnetic field. The magnetic field is produced by the motion of electric charges, electric current. The magnetic field causes the magnetic force associated with magnets. The theoretical implications of electromagnetism led to the development of special relativity by Albert Einstein in 1905; and from this it was shown that magnetic fields and electric fields are convertible with relative motion as a four vector and this led to their unification as electromagnetism. (CMS Physics TDR, 2006)

1.1.1.2. Strong Interaction

In particle physics, the strong interaction holds quarks and gluons together to form protons, neutrons and other particles. The strong interaction is one of the four fundamental interactions, along with gravitation, the electromagnetic force and the weak interaction. The strong interaction is also the force that binds protons and neutrons together. In this context it is called the nuclear force, and it is the residue strong interaction between the quarks that make up the protons and neutrons. The strong force is thought to be mediated by gluons, acting upon quarks, anti-quarks, and the gluons themselves. (CMS Physics TDR, 2006)

1.1.1.3. Weak Interaction

The weak interaction is one of the four fundamental interaction of nature. In the Standard Model of particle physics, it is due to the exchange of the heavy *W* and *Z* bosons. Its most familiar effect is beta decay and the associated radioactivity. The word weak derives from the fact that the typical field strength is 10^{-11} the strength of the electromagnetic force and some 10^{-13} that of the strong force, when forces are compared between particles interacting in more than one way. (CMS Physics TDR, 2006)

1.1.1.4. Gravitational Interaction

Gravitation is a natural phenomenon by which objects with mass attract one another. In everyday life, gravitation is most commonly thought of as the agency which lends weight to objects with mass. Gravitation causes dispersed matter to coalesce, thus accounting for the existence of the Earth, the Sun, and most of the macroscopic objects in the universe. It is responsible for keeping the Earth and the other planets in their orbits around the Sun; for keeping the Moon in its orbit around the Earth; for the formation of tides; for convection, by which fluid flow occurs under the influence of a density gradient and gravity; for heating the interiors of forming stars and planets to very high temperatures; and for various other phenomena observed on Earth. Modern physics describes gravitation using the general theory of relativity, in which gravitation is a consequence of the curvature of space-time which governs the motion of inertial objects. The simpler Newton’s law of universal gravitation provides an accurate approximation for most calculations.(CMS Physics TDR, 2006).

1.1.2. Fermions, Quarks, Leptons and Bosons

Fermions have half-integer spin; for all known elementary fermions this is ½. Fermions are particles which obey Fermi-Dirac statistics; they are named after Enrico Fermi. Each known fermion has its own distinct antiparticle.

Fermions are the basic building blocks of all matter. They are classified according to whether they interact via the color force or not. In the Standard Model, there are 12 types of elementary fermions: six quarks and six leptons.

Quarks are the fundamental constituents of hadrons and interact via the weak and electromagnetic interaction in addition to strong interaction. Quarks are the only known carriers of fractional charge, but because they combine in groups of three (baryons) or with their antiparticle (mesons), only integer charge is observed in nature. Their respective antiparticles are the anti- quarks which are identical except for the fact that they carry the opposite electric charge (for example the up quark carries charge $+^2\!/_3$, while the up anti-quark carries charge $-^2\!/_3$), color charge, and baryon number. There are six flavors of quarks; the three positively charged quarks are called up-type quarks and the three negatively charged quarks are called down-type quarks. For details you can see the table 1.1.

Table 1.1. Quarks

Name	Symbol	Antiparticle	Charge e	Mass (MeV/c^2)
up	u	$\bar{u}$	+⅔	1.5–3.3
down	d	$\bar{d}$	−⅓	3.5–6.0
charm	c	$\bar{c}$	+⅔	1,160–1,340
strange	s	$\bar{s}$	−⅓	70–130
top	t	$\bar{t}$	+⅔	169,100–173,300
bottom	b	$\bar{b}$	−⅓	4,130–4,370

Leptons do not interact via the strong interaction. Their respective antiparticles are the anti-leptons which are identical except for the fact that carry the opposite electric charge and lepton number (Table 1.2.). While the antiparticle of the electron is the anti-electron, it is nearly always called positron for historical reasons. There are six leptons in total; the three charged leptons are called electron-like leptons, while the neutral leptons are called neutrinos.

Table 1.2. Leptons

Name	**Symbol**	**Antiparticle**	**Charge e**	**Mass (MeV/c²)**
Electron	e^-	e^+	−1	0.511
Electron neutrino	ν_e	$\bar{n}_e$	0	< 2.2 eV/c^2
Muon	μ^-	μ^+	−1	105.7
Muon neutrino	ν_μ	$\bar{n}_m$	0	< 0.170
Tauon	τ^-	τ^+	−1	1777
Tauon neutrino	ν_τ	$\bar{n}_t$	0	< 15.5

Bosons have integer spin. The fundamental forces of nature are mediated by gauge bosons, and mass is hypothesized to be created by the Higgs boson. According to the Standard Model the elementary bosons are shown in Table 1.3.

Table 1.3. Bosons.

Name	**Symbol**	**Antiparticle**	**Charge (e)**	**Spin**	**Mass (GeV/c^2)**	**Interaction mediated**
Photon	γ	Self	0	1	0	Electromagnetism
W boson	W^-	W^+	−1	1	80.4	Weak interaction
Z boson	Z	Self	0	1	91.2	Weak interaction
Gluon	g	Self	0	1	0	Strong interaction
Higgs boson	H^0	Self?	0	0	> 112	None
Graviton	G	Self	0	2	0	Gravitation

The Standard Model makes several predictions about the universe, many of which seem to be true according to various experiments. But there are other aspects of the model that remain unproven. One of those is a theoretical particle called the Higgs boson particle (shown in Table 1.3.). (CMS Physics TDR, 2006)

1.1.3. The Higgs Boson

The Higgs boson is a massive scalar elementary particle predicted to exist by the Standard Model in particle physics. (CMS Physics Note, 2006) At present there are no known fundamental scalar particles in nature. The Higgs boson is the only Standard Model particle that has not yet been observed. Experimental detection of the Higgs boson would help explain the origin of mass in the universe. More specifically, the Higgs boson would explain the difference between the massless photon, which mediates electromagnetism, and the massive W and Z bosons, which mediate the weak force. Assuming that the Higgs boson exists, it is expected to be discovered at the Large Hadron Collider. Moreover, the Minimal Supersymmetric

Standard Model (MSSM) predicts several Higgs bosons. (P.W. Anderson, 1963) The Higgs mechanism, which gives mass to vector bosons, was theorized in 1964 by Francois Englert and Robert Brout; (Comptes Rendus Physique, 2007) in October of the same year by Peter Higgs, working from the ideas of Philip Anderson (P.W. Anderson, 1963) and independently by Geraid Gurainik, C.R. Hagen, and Tom Kibble (P.W. Higgs, Phys. Rev. Lett, 1964), who worked out the results by the spring of 1963. (D'Enterria, 2007)

1.1.4. Composite Particles

1.1.4.1. Hadrons

Hadrons are defined as strongly interacting composite particles. Hadrons are either;

-Composite fermions, in which case they are called baryons.

-Composite bosons, in which case they are called mesons.

Baryons; are the family of composite particles made of three quarks, as opposed to the mesons which are the family of composite particles made of one quark and one anti-quark. Both baryons and mesons are part of the larger particle family comprising all particles made of quarks-the hadrons. The term baryon is derived from the Greek, meaning "heavy", because at the time of their naming it was believed that baryons were characterized by having greater masses than other particles.Since baryons are composed of quarks, they participate in the strong interaction. Leptons, are not composed of quarks and as such do not participate in the strong interaction. The most well known baryons are the protons and neutrons which make up most of the mass of the visible matter in the universe, whereas electrons are leptons. For example, Protons, composed of two up and one down quark (*uud*) and neutrons, composed of two down and one up quark (*ddu*). Also each baryon has a corresponding antiparticle, the antiproton, is made of two up and one down anti-quarks. (CMS Physics TDR, 2006).

1.1.4.2. Mesons

In particle physics, mesons are subatomic particles composed of one quark and one anti-quark. The main difference between mesons and baryons is that mesons are bosons while baryons are fermions that is mesons have integer spin while baryons have half- integer spin meaning that the Pauli exclusion principle does not apply to mesons. Since mesons are composed of quarks, they participate in both the weak and strong interactions. Mesons with net electric charge also participate in the electromagnetic interaction. They are classified according to their quark content, total angular momentum, parity, and various other properties such as C-parity and G-parity. While no meson is stable, those of lower mass are nonetheless more stable than the most massive mesons, and are easier to observe and study in particle accelerators or in cosmic ray experiments. (CMS Physics TDR, 2006).

1.2. Large Hadron Collider

The Large Hadron Collider (LHC) is the world's largest and highest-energy particle accelerator, intended to collide opposing particle beams, of either protons at an energy of 7 TeV per particle and luminosities up to 10^{34} $cm^{-2}s^{-1}$ (Pb-Pb collisions have 1312 GeV and luminosities up to 10^{27} $cm^{-2}s^{-1}$). The Large Hadron Collider was built by the European Organization for Nuclear Research (CERN) with the intention of testing various predictions of high-energy physics, including the existence of the hypothesized Higgs boson and of the large family of new particles predicted by supersymmetry. The Large Hadron Collider (LHC) is being built in the circular LEP tunnel with 27 km in circumference (shown Figure 1.1.).

The tunnel is buried around 50 to 175 m. underground.

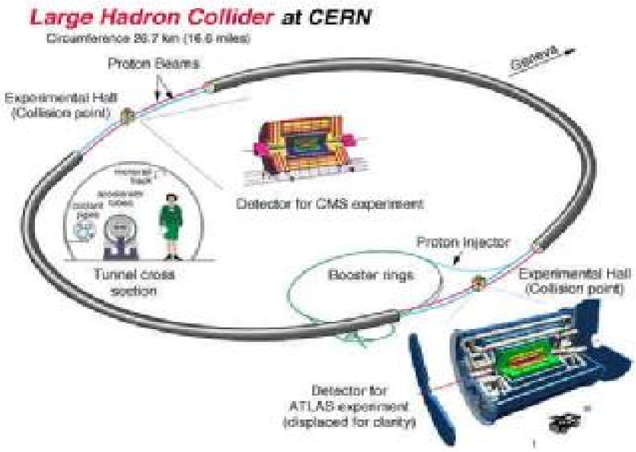

Figure 1.1. Large Hadron Collider at CERN

The beam moves around the LHC ring inside a continuous vacuum chamber which passes through a large number of magnets. 1232 dipole magnets bend the beam around the 27 km. ring. The momentum of the beam is very high and these magnets have to produce a very strong magnetic field. To reach the high magnetic field required, high currents are needed. The cables of the magnets are of a very special design and conduct current without resistance in their superconducting state. The beams will be stored at high energy for 10 to 20 hours. In 10 hours the particles make four hundred million revolutions around the machine.

Although the Standard Model (SM) of particle physics has so far been tested to exquisite precision, it is considered to be an effective theory up to TeV scale. The goal of High Energy Physics is to answer these questions: what are the fundamental constituents of matter and what are the fundamental forces controlling the behavior of matter? In order to answer these questions, we need to identify the intrinsic features and characteristics of particles at the basic level. For this, we need to employ well-defined devices to prove physical models. The LHC at CERN is the largest accelerator in the world where different detectors will operate.

Six detectors have been constructed at the LHC, located underground in large caverns excavated at the LHC's intersection points. Two of them, the ATLAS experiment will be used to look for signs of new physics, including the origins of mass and extra dimensions, and the Compact Muon Solenoid (CMS) will, like ATLAS, hunt for the Higgs boson and look for clues to the nature of dark matter, A Large Ion Collider Experiment (ALICE) will study a "liquid" form of matter called quark-gluon plasma that existed shortly after the Big Bang, and while LHCb will search to answer although equal amounts of matter and antimatter were created in the Bing Bang why we only see a universe which consists of only matter. ALICE and LHCb have more specific roles and the last two TOTEM and LHCf are smaller than others and are for very specialized research. (CMS Physics TDR, 2006)

1.3. Compact Muon Solenoid

CMS (Compact Muon Solenoid) is one of the detectors which will be operating at the LHC. CMS is designed as a general-purpose detector to investigate a wide range of physics. The CMS detector is built around a huge solenoid magnet. This takes the form of a cylindrical coil of superconducting cable that generates a magnetic field of 4 Teslas, about 100 000 times that of the earth. It contains sub-systems which are designed to measure the energy and momentum of photons, electrons, muons, and other product of the collisions. The main goals of the experiment are; to explore physics at the TeV scale, to discover the Higgs boson, to look for evidence of physics beyond the standard model, such as super symmetry, or extra dimensions, to study aspects of heavy ion collisions and to study Quantum Chromo Dynamics (QCD) in extreme conditions of temperature and density produced in Pb-Pb collisions. An overall picture of the CMS can be seen in Figure 1.2.

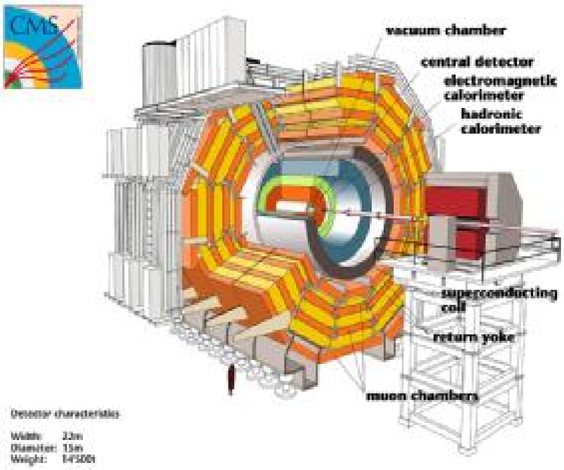

Figure 1.2. The CMS detector (The CMS Collaboration, 2008)

The CMS detector consists of a silicon tracker, an electromagnetic calorimeter, and a hadron calorimeter, surrounded by a high field superconducting solenoid, muon detectors, as well as forward sampling calorimeters, it covers most of the 4π solid angle and a wide pseudo rapidity range. The CASTOR (Centauro and Strange Object Research) calorimeter is one of the forward detectors of CMS which is dedicated to the search of Centauro-type events in heavy-ion collisions, related to previous exotic cosmic ray phenomena which have been studied in many experiments. (CMS Physics TDR, 2006)

1.3.1. The Tracker

Immediately around the interaction point the inner tracker serves to identify the tracks of individual particles and match them to the vertices from which they originated. The curvature of charged particle tracks in the magnetic field allows their charge and momentum to be measured. The CMS silicon tracker consist of 13 layers in the central region and 14 layers in the end caps. The innermost three layers consist of 100 × 150 µm pixels, 66 million in total. The next four layers (up to 55 cm radius) consist of 10 cm × 180 µm silicon strips, followed by the remaining six layers of 25 cm ×180 µm strips, out to a radius of 1.1 m. There are 9.6 million strip channels in total. During full luminosity collisions the occupancy of the pixel layers per event is expected to be 0.1%, and 1-2% in the strip layers. Figure 1.3. shows the CMS tracking system. (CMS Physics TDR, 2006)

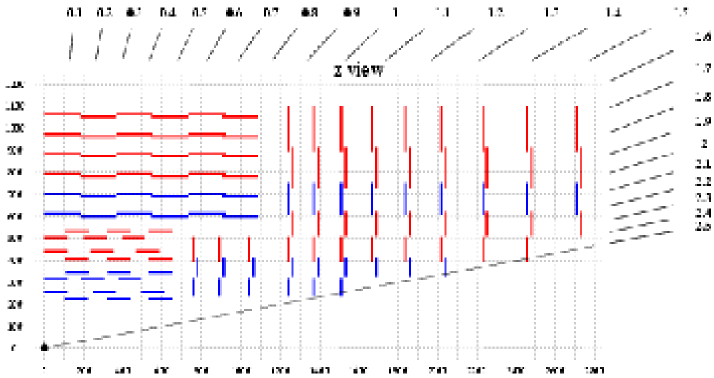

Fig.1.3. CMS Tracker System

1.3.2. Electromagnetic Calorimeters

Electromagnetic calorimeters are specifically designed to measure the energy of particles that interact primarily via the electromagnetic interaction. With its over 80,000 scintillation lead tungsten $PbWO_4$ (PWO) crystals the CMS electromagnetic calorimeter (ECAL) will be the largest one ever constructed. It was designed to work in the demanding LHC environment and give a resolution of a 0.5% for photon energies above 50 GeV/c. Of particular interest are electrons and photons, because of their use in finding the Higgs boson and other new physics. Lead tungsten crystal is made primarily of metal and is heavier than stainless steel, but with a touch of oxygen in this crystalline form it is highly transparent and “scintillates” when electrons and photons pass through it. This means it produces light in proportion to the particle’s energy. These high-density crystals produce light in fast, short, well-defined photon bursts that allow for a precise, fast and fairly compact detector. The layout of the CMS ECAL is shown in Figure 1.4. (CMS Physics TDR, 2006)

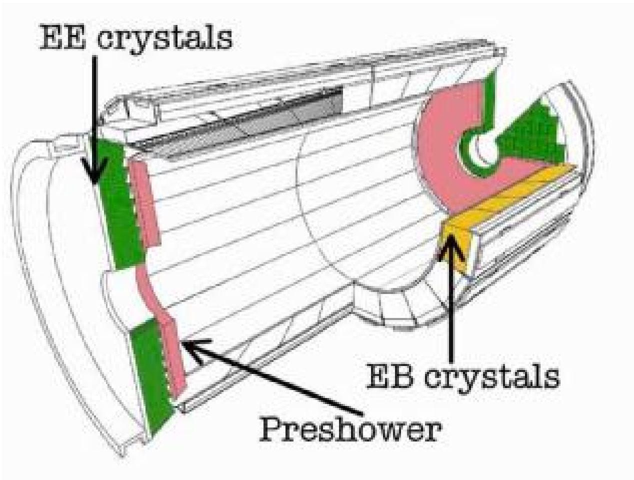

Figure 1.4. CMS ECAL.

1.3.3. Hadronic Calorimeter

The Hadronic Calorimeter (HCAL), plays an essential role in the identification and measurement of quarks, gluons, and neutrinos by measuring the energy and direction of jets and of missing transverse energy flow in events. Missing energy forms a crucial signature of new particles, like the super symmetric partners of quarks and gluons. For good missing energy resolution, a hermetic calorimetry coverage of eta=5 is required.

The HCAL also aids in the identification of electrons, photons and muons in conjunction with the tracker, electromagnetic calorimeter, and muon systems.

The barrel, or central detector, is a cylindrical structure which surrounds the collision region and measures the energy of quarks and jets emerging at large angles relative to the beam direction. The end cap calorimeters look like end-plugs and enclose the ends of the barrel region.

To accomplish this feat, the HCAL is organized into barrel (HB and HO), end cap (HE) and forward (HF) sections. There are 36 barrel “wedges”, each weighing 26 tones.

These form the last layer of detector inside the magnet coil whilst a few additional layers, the outer barrel (HO) ,which covers the region -1.26< $|\eta|$ <1.26, sit outside the coil, ensuring no energy leaks out the back of the HB undetected, the HCAL end caps (HE) cover the pseudo rapidity range 1.3< $|\eta|$ <3.0 and HB covers the range -1.4< $|\eta|$ <1.4. Lastly, the two hadronic forward calorimeters HF is located at 3.0< $|\eta|$ <5.0. (CMS Physics TDR, 2007).

1.3.4. The Magnet

The CMS magnet is the central device around which the experiment is built, with a 4 Tesla magnetic field is 100, 000 times stronger than the Earth’s. Its job is to bend the paths of particles emerging from high-energy collisions in the LHC. The more momentum a particle has the less its path is curved by the magnetic field, so tracing its path gives a measure of momentum. CMS began with the aim of having the strongest magnet possible because a higher strength field bends paths more and, combined with high-precision position measurements in the tracker and muon detectors, this allows accurate measurement of the momentum of even high-energy particles. (CMS Physics TDR, 2007)

1.3.5. The Muon System

As the name “Compact Muon Solenoid” suggests, detecting muons is one of CMS’s most important tasks. Muons are charged particles that are just like electrons and positrons, but are 200 times heavier. We expect them to be produced in the decay of a number of potential new particles; for instance, one of the clearest “signatures” of the Higgs Boson is its decay into four muons. Because muons can penetrate several meters of iron without interaction, unlike most particles they are not stopped by any of CMS's calorimeters. Therefore, chambers to detect muons are placed at the very edge of the experiment where they are the only particles likely to register a signal. (CMS Physics TDR, 2007)

1.4. CMS Forward Detectors

There are three forward detectors, HF, CASTOR and ZDC, in CMS experiment. They are very important detectors due to their pseudo rapidity ranges, which shown in Figure 1.5. With their inclusion CMS become almost fully hermetic detector.

Çukurova University High Energy group has made very important contributions to HF and CASTOR from their construction to installation to the LHC beam line. This study is part of this contribution.

Forward detectors of CMS cover a wide range of physics subjects, including very low-x_{Bj} *QCD*, underlying event and multiple interactions characteristics, g-mediated processes, shower development at the energy scale of primary cosmic ray interactions with the atmosphere, diffraction in the presence of a hard scale and even Higgs discovery in central exclusive production. (CMS Physics TDR, 2007)

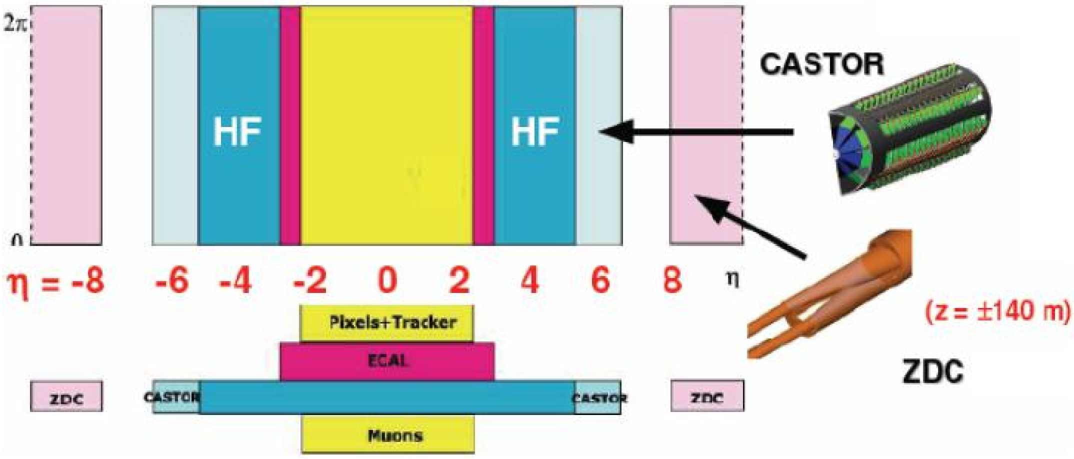

Figure 1.5. Pseudorapidity-azimuth coverage of the full CMS detector (CASTOR EDR, 2007).

1.4.1. The Hadron Forward Calorimeter of the CMS experiment at the LHC

The forward calorimeters in the Compact Muon Solenoid (CMS) experiment at the Large Hadron Collider (LHC) cover a large pseudo rapidity range, $3 < \eta < 5$, and thus significantly improve jet detection and the missing transverse energy resolution which are essential in top quark production studies, Standard Model Higgs, and all SUSY particle searches. Higgs boson production through weak boson fusion as a potential Higgs discovery channel requires identification of high energy quark jets by the forward calorimeters. This channel is largely characterized by two energetic forward tagging jets $(<p>) = 1$ TeV with a typical transverse momentum of $m_w/2$ .The largest suppression against background is achieved by the efficient identification of these tagging jets by two forward calorimeters.

The forward calorimeter will experience unprecedented particle fluxes. On average, 76 GeV per proton-proton interaction is deposited into the two forward calorimeters, compared to only 100 GeV for the rest of the detector. At $\eta=5$ and integrated luminosity of 5×10^5 pb^{-1} (~10 year of LHC operation), the HF will experience ~1 Grad. This hostile environment presents a considerable challenge to calorimetry, and the design of the HF calorimeter was first and foremost guided by the necessity to survive in these harsh conditions. Successful operation critically depends on the radiation hardness of the active material. This was the principal reason why quartz fibers were chosen as the active medium. The signal is generated when charged shower particles has energy above the Cerenkov threshold (E > 190 KeV for electrons), the calorimeter mostly sensitive to the electromagnetic component of showers. Fibers are inserted in these grooves. The detector is functionally subdivided into two longitudinal segments. Half of the fibers run over the full depth of the absorber (165 cm = 10 λ_I while the other half starts at a depth of 22 cm from the front of the detector. These two sets of fibers are read out separately. This arrangement makes it possible to distinguish showers generated by electrons and photons, which deposit a large fraction of their energy in the first 22 cm, from those generated by hadrons, which produce nearly equal signals in both calorimeter segments on average. The long fiber section is referred as L (measuring the total signal), and the short fiber section as S (measuring the energy deposition after 22 cm of steel).

The forward calorimeter is essentially a cylindrical steel structure with an outer radius of 130.0 cm. The front face of the calorimeter is located at 11.2 m from the interaction point. The hole for the beam pipe is cylindrical, with radius 12.5 cm from the center of the beam line. This structure is azimuthally subdivided into 20^0 modular wedges. Thirty-six such wedges (18 on either side of the interaction point) make up the HF calorimeters. The fibers run parallel to the beam line, and are bundled to form 0.175×0.175 in $\Delta\eta \times \Delta\varphi$ towers . The detector is housed in a hermetic radiation shielding which consists of layers of 40 cm thick steel, 40 cm of concrete, and 5 cm of polyethylene. The inner part of HF will experience radiation doses close to 100 Mrad/year, and large neutron fluxes leading to activation of the absorber material, reaching several mSv/h in the region closest to the beam line after 60 days of running at 10^{34} cm^{-2} s^{-1} luminosity and one day of cooling down. The HF calorimeter covers a large pseudo rapidity region ($3 < \eta < 5$), and is essential for large number of physics channels with missing transverse energy.

The active elements of HF (quartz fibers) are sufficiently radiation-hard to survive these levels of radiation with limited deterioration. A 10-cm-thick lead plate, located in front of HF during operations around the detector, reduces personal exposure to radiation from the absorber.

Maintenance of read-out boxes will be performed with the help of semi-automatic extractor tools. HF is equipped with radiation monitors located at the periphery of the detector, and with a system (Raddam) to measure the transmission properties of a few reference quartz fibers embedded in the absorber, as a function of integrated luminosity. The recovery is maximum at 450 nm which is also the maximum of PMT HF efficiency.

Table 1.4. The tower sizes, number of fibers, bundle sizes and the percentage of photocathode area utilized are listed below for each tower.(CMS NOTE, 2006).

Ring No	**r_{in},r_{out}(mm)**	Δh	Δf **(deree)**	**N_{fib}**	**A_{bundle} (mm^2)**	**A_{bundle}/ $A_{photocathode}$**
1	**(1162-1300)**	**0.111**	**10**	**594**	**551**	**1.14**
2	**(975-1162)**	**0.175**	**10**	**696**	**652**	**1.33**
3	**(818-975)**	**0.175**	**10**	**491**	**469**	**0.96**
4	**(686-818)**	**0.175**	**10**	**346**	**324**	**0.66**
5	**(576-686)**	**0.175**	**10**	**242**	**231**	**0.47**
6	**(483-576)**	**0.175**	**10**	**171**	**167**	**0.34**
7	**(406-483)**	**0.175**	**10**	**120**	**120**	**0.25**
8	**(340-406)**	**0.175**	**10**	**85**	**88**	**0.18**
9	**(286-340)**	**0.175**	**10**	**59**	**63**	**0.13**
10	**(240-286)**	**0.175**	**10**	**41**	**46**	**0.94**
11	**(201-240)**	**0.175**	**10**	**30**	**35**	**0.71**
12	**(169-201)**	**0.175**	**20**	**42**	**52**	**0.11**
13	**(125-169)**	**0.300**	**20**	**45**	**50**	**0.10**

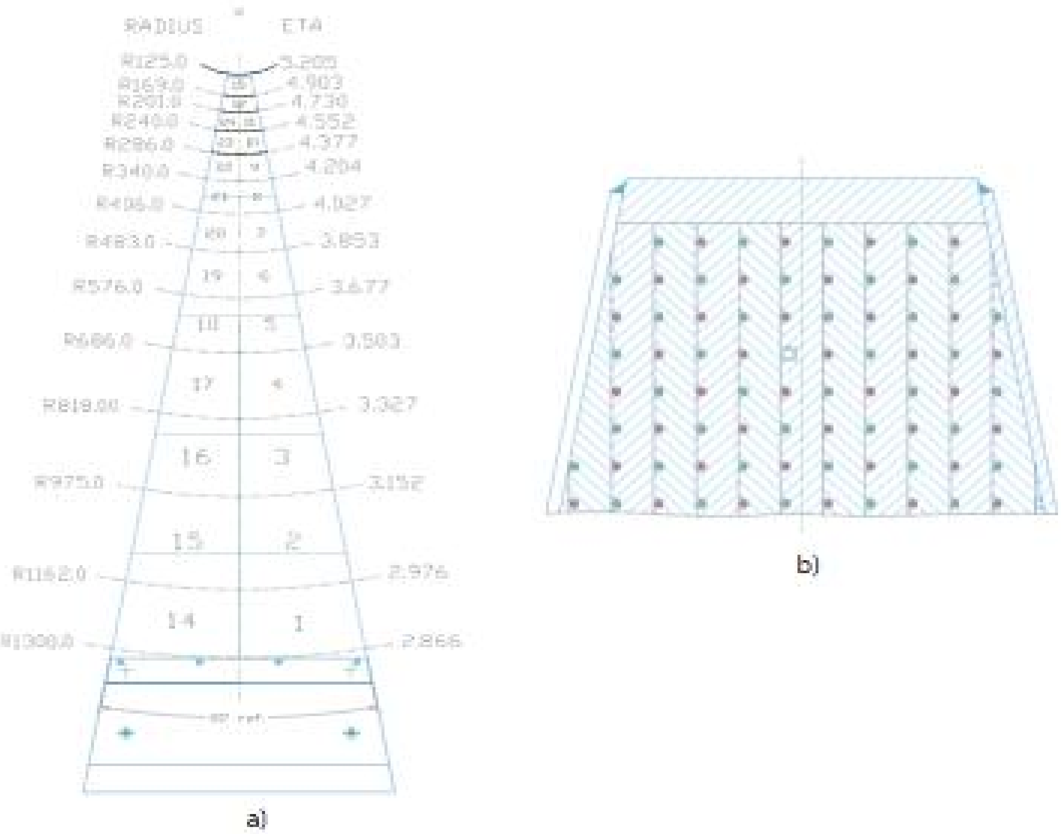

Figure 1.6. Wedge near the beam pipe (a), long and short fibers sapareted by 5 mm (b) , (CMS NOTE, 2006)

The transverse segmentation (Figure 1.6.) is 0.175 × 0.175 in $\Delta\eta \times \Delta\varphi$ with the exception of two towers (12 and 13) at the tip of the wedge near the beam pipe (a). An expanded view of tower 13 shows the radioactive source tube in the center of the tower. Long and short fibers alternate and are separated by 5 mm (b). (CMS NOTE, 2006).

1.4.2. CASTOR Forward Detector of CMS Experiment

CASTOR calorimeter has an electromagnetic (EM) and hadronic (HAD) parts and segmented as 16-fold azimuthally symmetric structure around the beam pipe. It is also longitudinally segmented into 14 sections, 2 for the EM and remaining are for the HAD parts. Figure 1.7. shows the schematic design drawing of the calorimeter. The calorimeter is constructed in layers of tungsten (W) plates as absorber and fused silica quartz (*Q*) plates as active medium. The signal is the Cherenkov light produced by the passage of the charged particles in the shower through the quartz medium. These *W/Q*-layers are inclined at 45 ^{o} from the beam direction, in order to maximize the Cherenkov light output. The refraction index of quartz is n =1.46-1.55 for wavelengths l = 200-600 nm. The corresponding Cherenkov threshold velocity *is* $b_c = 1/n$ = 0.65-0.69, for b_c ~1 the angle of emission is $q_c = a\cos(1/n\ b)$ = 46^{o}-50^{o} . The calorimeter has 16 x 14 subdivisions (224 channels in total) and the light produced in each one is collected and focused by air-core light guides onto the corresponding PMTs.

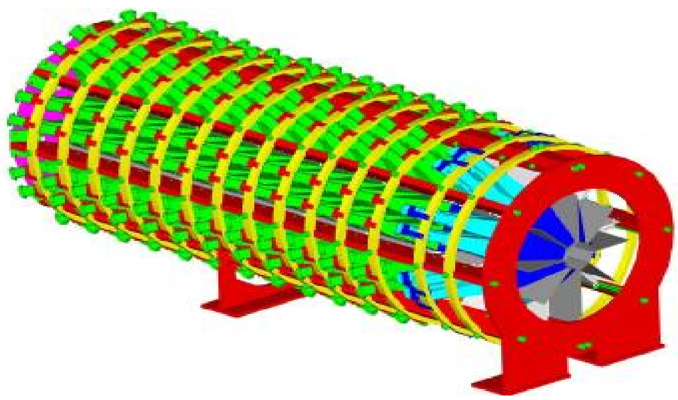

Figure 1.7. Schematic design of the full CASTOR calorimeter simulated with MC.(CASTOR EDR, 2007)

The calorimeter will be situated at 14,385 m from the interaction point, subtending the pseudo rapidity range $5.3 < \eta < 6.6$. The calorimeter is divided into an electromagnetic and a hadronic section, Figure 1.8. The electromagnetic section has 2 x 16 channels and depth 2 x 10=20 radiation lengths, Xo , or 0.77 interaction lengths λ_I. Each channel (readout unit,RU) consist of 5 tungsten and 5 quartz plates of thickness 5 mm and 2 mm, respectively. The hadronic section has 12 x 16 channels and depth 12 x 0.77 λ_I . Each RU consists of 5 tungsten and 5 quartz plates of thickness 10 mm and 4 mm, respectively. The calorimeter has total depth 10 λ_I .

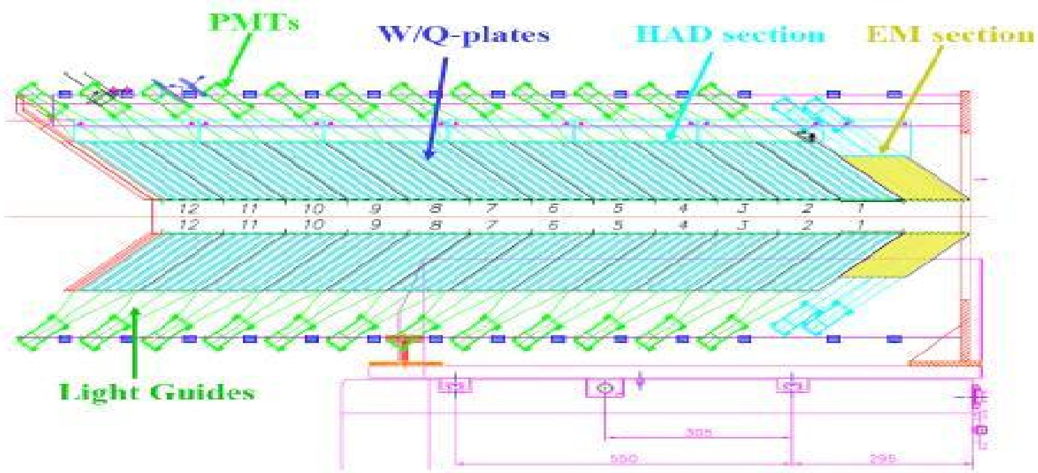

Figure 1.8. Schematic longitudinal view of the CASTOR Calorimeter design (see CASTOR EDR, 2007).

The calorimeter will be positioned at 14.385 m from the interaction point. As we mentioned above, covering the pseudo rapidity range of $5.1 \leq \eta \leq 6.6$, the η-range covered will be $5.3 \leq |\eta| \leq 6.46$ for the electromagnetic section with 99% containment and $5.25 \leq |\eta| \leq 6.31$ for the hadronic section with 95% containment.The later η range provides complete overlap with the HF calorimeter. (CASTOR EDR, 2007)

1.4.3. ZDC Forward Detector of CMS Experiment

The Zero Degree Calorimeter (ZDC) is a sub-system of the CMS Forward HCAL. The Zero Degree Calorimeter will be downstream of the first beam dipole magnets at the straight section and between the two beam pipes at ~140 m on each side of the interaction vertex. The ZDC are able to measure the energy of forward neutrons and photons since these are not deflected by the bending magnets. The ZDCs will improve the collision centrality determination while CASTOR, covering $5.3< \eta<6.7$, studies charged particles and electromagnetic energy fluctuations and gluon saturation/colour-glass-condensate phenomena at very low x, $10^{-5} < x < 10^{-7}$. (CASTOR EDR, 2007).

1.4.4. Forward Physics in CMS

The LHC will be the first accelerator to effectively probe the very high energy cosmic ray domain, close to the end of the cosmic ray spectrum. Both experimental data and model predictions indicate that the forward rapidity region (~ 5< η<7) is the most favorable place for the production of low-*x* QCD, ultra-high-energy cosmic-rays, Higgs production and electro-weak measurement. The physics program for CASTOR and HF as part of CMS now goes beyond the study of cosmic ray phenomena and will be used in both pp and HI physics in general. It will provide information on the following topics:

- QCD Oriented Physics
- Low-*x* QCD physics; Parton Saturation
- Diffractive QCD
- Hadronization
- Higgs physics
- BSM physics

In general, the addition of CASTOR to the CMS experiment results in a substantial enhancement of its physics potential, as several important observations in *p-p, p-Pb* and *Pb-Pb* interactions would either be impossible or seriously diminished without CASTOR. Originally designed as a calorimeter dedicated to the search of exotic events in heavy ion collisions, CASTOR has a rather broad physics program, associated with the very forward rapidity region. It will contribute mainly to the QCD studies, such as diffractive, low-*x* physics and multi-Parton interactions, offering the ability to test the non perturbative region of QCD at Bjorken-*x* of the order of 10^{-6}–10^{-7}, as well as to Quark-Gluon Plasma and cosmic-ray physics topics as well as HF. Of special interest are also specific discovery physics topics associated with Higgs, BSM studies and strangelets. (CASTOR EDR, 2007).

1.4.4.1. QCD Oriented Physics

The study of the fundamental theory of the strong interaction – Quantum Chromo dynamics (*QCD*) – in extreme conditions of temperature, density and Parton momentum fraction (low-*x*) has attracted an increasing experimental and theoretical interest during the last 20 years. Indeed, *QCD* is not only a quantum field theory with an extremely rich dynamical content such as asymptotic freedom, infrared slavery, nontrivial vacuum topology, strong *CP* violation problem, $U_A(1)$ axial-vector anomaly, color superconductivity *pp* collisions, multiple interactions can occur between the partons of the colliding beam protons, hence we can distinguish between a “hard scattering” component, i.e. the two outgoing hard jets and the so called "underlying event" which consists of the beam-beam remnants plus initial and final-state radiation. Multiple Parton scattering contributes to the "underlying event", adding an uncertainty in the interpretation of certain hadronic final states which could be produced either by new physics (*Higgs* or *SUSY*) or via multiple Parton interactions. Energy-flow measurements as well as trigger on the deposited energy in CASTOR will serve as a tool for the better understanding of the dynamics of multiple interactions and the structure of the underlying event, further helping to tune existing MC *QCD* generators. (CASTOR EDR, 2007).

1.4.4.2. Low-*x* Physics; Parton Saturation

The idea of saturation of parton densities in small *x* physics is introduced. The most compelling indirect evidence of saturation comes from the phenomenological success of some models containing saturation ideas when confronted to *HERA* data. The most commonly used is the *GBW* model. At LHC energies, the gluon density will be so large that non-linear (gluon-gluon fusion) effects will become important, saturation the growth of the Parton densities the transition to the regime of saturated *PDFs* is expected for small x values ($x < 10^{-4}$). Processes such as jets and Drell Yan (*DY*) production, in the region η=5-6 will allow to access low-x region ($x_{BJ} \sim 10^{6}$). The measurement of forward jets ($pp \rightarrow j\ X$) or Drell-Yan pairs ($pp \rightarrow l^{+} l^{-} X$) within CASTOR's and HF's eta coverage offers the possibility to study the proton Parton Distribution Functions (*PDFs*) of the proton at very small parton momentum fractions ($x \sim 10^{-6}$). (Heavy Ion Physics TDR, 2007).

1.4.4.3. Diffractive QCD

Diffraction, traditionally thought of as soft process, can occur with a hard scale (*W*, dijets, heavy flavors) as has been experimentally observed at *UA8*, *HERA* and Tevatron. In the presence of a hard scale, diffractive processes can be described in perturbative *QCD* (*pQCD*) and their cross sections can be factorized into that one of the hard scatter and a diffractive particle distribution function (*dPDF*). Single diffractive *W* production, ($pp \rightarrow pX$), where X includes a W, is an example for diffraction with a hard scale at the LHC and is in particular sensitive to the quark component of the proton *dPDF* in an as-of-yet unmeasured region. In the absence of event pile-up, a selection is possible based on the requirement that there be no activity above noise level in the CMS forward calorimeters CASTOR and HF.

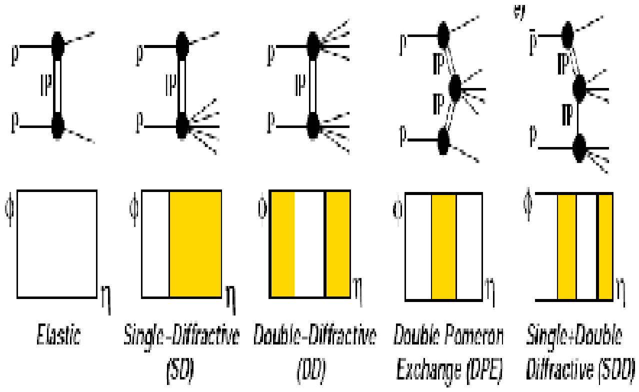

Figure 1.9. Rapidity gaps for diffractive scattering (D'Enterria, 2007)

1.4.4.4. Hadronization

The Centauro fireball finally can decay into non-strange baryons and strangelet(s) having very high strangeness. The strangelet temperature is expected to be lower than that estimated for Centauro fireball. The independent hadronization (*IH*) model of Field is the simplest such model to implement. In this picture, a new quark-antiquark pair can be created in the color field of the parent quark q_0 . Then the quark anti-quark pair can turn into a meson with a longitudinal momentum fraction described by a phenomenological function, with the remainder of the longitudinal momentum carried by the quark q_1 . This process is repeated by the creation of *a* $q_2\bar{q}_2$. A host of mesons are thus produced, and decayed to the quasi-stable π, K…..mesons according to their experimental properties. The final residual quark q_n will have very little energy, and can be discarded without significantly affecting jet physics. (Gladysz-Dziadus, 2001)

1.4.4.5. Higgs Physics

The primary focus of proton-proton collisions at the LHC is to search for the Higgs boson and for physics beyond the standard model, such as super symmetric partners to the currently known particles. Because of the very high luminosities required to reveal rare phenomena, the CASTOR and HF calorimeter will not be particularly useful in this specific study. However, it can be used to provide important practical and fundamental contributions to the proton-proton program. Because of the fast response and relatively large deposited energy, CASTOR and HF may be useful as a luminosity monitor in the early stages of LHC machine development. (D' Enterria, 2007).

2. MATERIAL AND METHOD

2.1. The HF Online Radiation Damage Monitoring (Raddam) System

As explained in section 1.4.1 HF detector will be subject to tremendous amount of radiation. Due that that it is very important to know how the fibers are effected from the radiation. Turkish High Energy group with collaboration with Iowa HEP group proposed to install a system to monitor online radiation damage of HF fibers. These system will be explained in detail in below section.

The system is based upon the idea that the ratio of the pulses which come from the first reflection point (which is not effected much by radiation) and from the light reflected at the end of the HF fiber which will be effected by the radiation. Measuring constantly the ratio of those two signals, one can monitor the radiation damage on the fibers.

It is important to know the effect of radiation. In the following section the test results of radiation damage on fiber will be explained. These studies also carried out by our group with collaboration with other Turkish institutes and university of Iowa group.

2.1.1. Radiation Damage of Fibers

These test were done using radiation test facilities at CERN. At this facility it is possible to send electrons or protons to fibers and measure the how optical transmittance of the fiber under the test changes due to absorbed dose.

According to results of these tests, when HF quartz fibers were irradiated, they exhibit a damage increasing with dose. The light absorption is very high below 380 nm, quite low near 450 nm, comparably high at 600 nm and negligible above 750 nm. When radiation is stopped the fiber starts to recover. Then transmitted signal starts to increase (Dumanoğlu et al., 2002 and Cankoçak et al., 2007). The two effects (radiation damage during the beam and recovery after radiation stops) can be parameterized (see the cited papers for detail). According the light attenuation $A(l,D)$ in the fibre at the dose D is well represented by the following function:

$$A(l,D) = a(l)[D/D_s]^{b(l)} \qquad (2.1.)$$

a and b parameters for qq and qp fibers are determined by fitting the ratios as a function of wavelength and dose.

$$I(l,D)/I(l,0) = \exp[-(L/4.343)a(l)(D/D_s)^{b(l)}] \qquad (2.2.)$$

Choosing a scale factor D_s = 100 Mrad, and L being expressed in meters, a is the attenuation at 100 Mrad, in dB/m. The results for qq and qp fibers are shown in Figures 2.1 and 2.2.

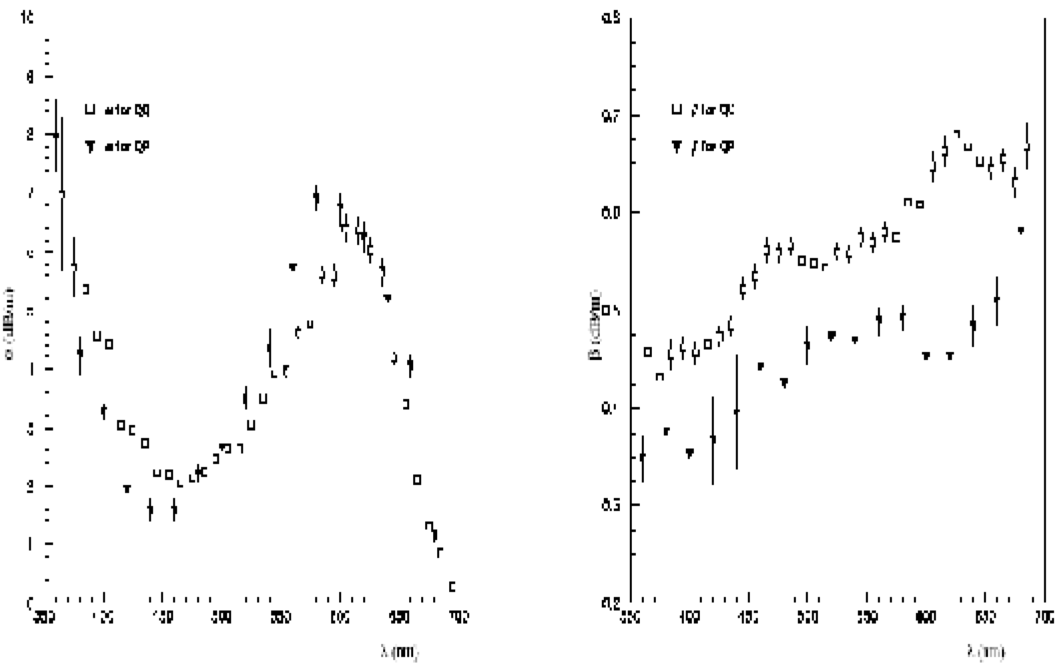

Figure 2.1. Radiation damage in quartz fibers which are irradiated by protons (Cankocak et al., CMS note, 2007).

The fiber radiation damage induced by protons exhibits the same well-known behavior as with electrons (compare the Figure 2.1. and 2.2), high light attenuation below 380 nm and in the band 550-680 nm. Moderate attenuation in the band 400-520 nm and practically no attenuation below 700 nm were observed. The damage varies exponentially with dose; fast in the first hours and slow after.

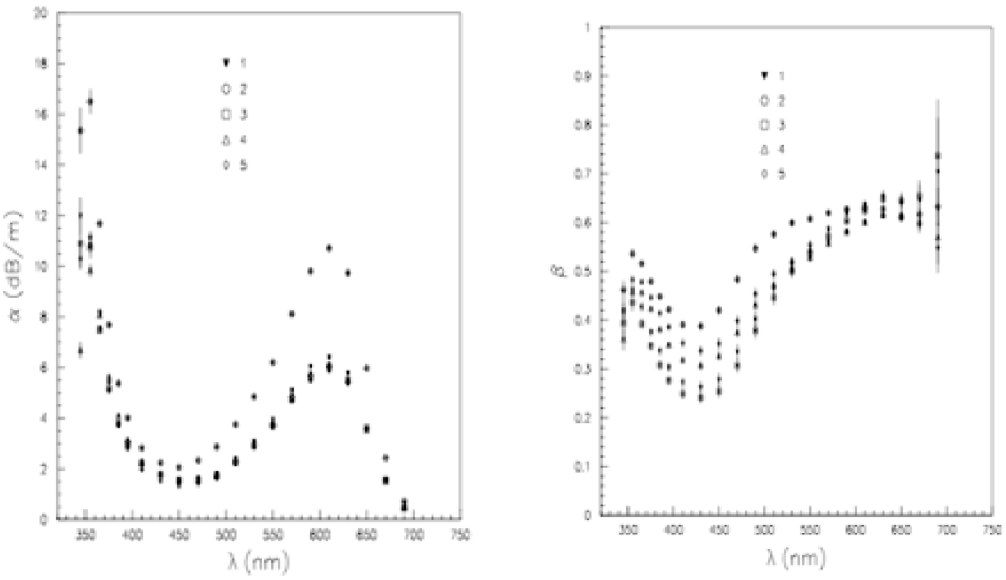

Figure 2.2. Radiation damage in quartz fibers which are irradiated by electrons (Dumanoglu et al., 2002).

2.1.2. Monitoring the Radiation Damage of Fibers

"CMS-HF is an iron-fiber calorimeter whose working principle depends on Cerenkov mechanism. The produced Cerenkov light is detected by PMTs whose sensitive range is in the 400-500 nm region. The knowledge of the evolution of light transmission in fibers during the working period due to irradiation and after a break in data taking due to recovery effect is important for the calibration of the detector. In order to monitor the radiation damage, the Raddam system is constructed using 56 HF fibers in different wedges.

The light is injected through a thin fiber which is glued side by side inside a capillary tube to the another fiber whose carry the reflected signal to the PMT. At the opposite side of the capillary the 2.5 m long Raddam fiber is placed (see Figure 2.3.). Raddam fiber has same length as other regular HF fibers. A blue light (~440 nm) which is shifted from a pulsed nitrogen laser (337 nm) light is used since blue corresponds to the PMT's most sensitive wavelength region. Reflection occur at the two ends (which are polished to get good reflection) of the Raddam fiber. S_1 is first reflection at the entrance and is almost independent of dose, while S_2 is second reflection at the far end of the fiber. There is 25 ns time separation between S_2 and S_1 since S_2 travel 5m fiber length till it comes to front end where first reflection occurs. Amplitude of S_2 depends on the transparency of the Raddam fiber, which is related to radiation damage, and recovery of it. Then the ratio $R=S_1/S_2$ gives measure of the transparency of the fiber.

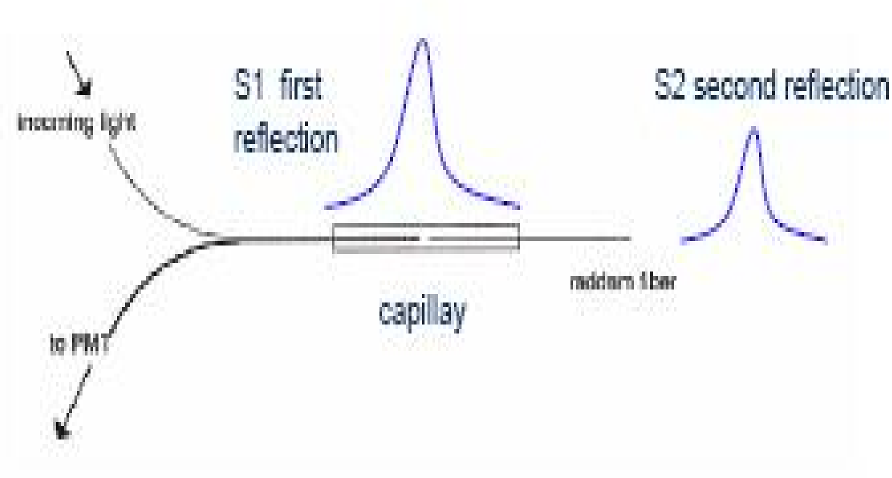

Figure 2.3. Raddam System.

The Raddam fiber is coupled with a small gap to the fiber, which carries the incoming laser light, and the fiber, which carries the reflected lights to the PMT, inside a capillary (Fig. 2.4.).

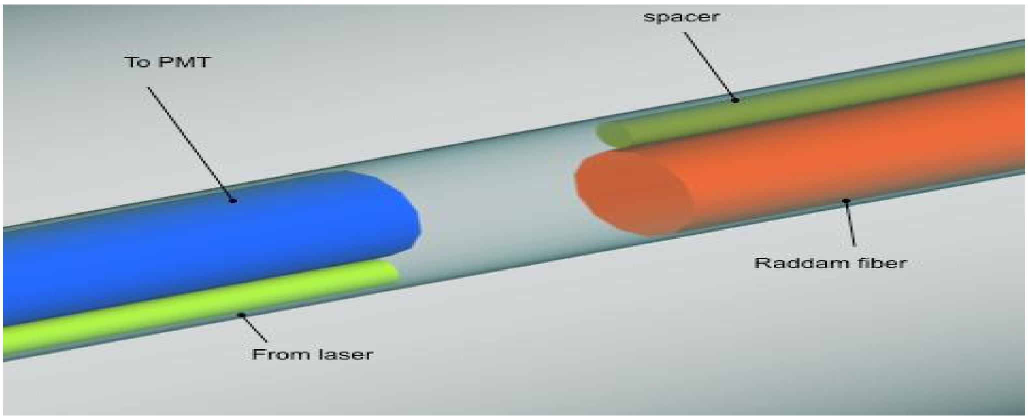

Fig 2.4. Fiber coupling in capillary.

Seven Raddam fibers were installed in each wedge, and there are totally 56 sample fibers in the entire system which will provide radiation damage information (see Figure 2.5.). Each fiber is readout by a PMT which also serves as a read out element of that particular tower.

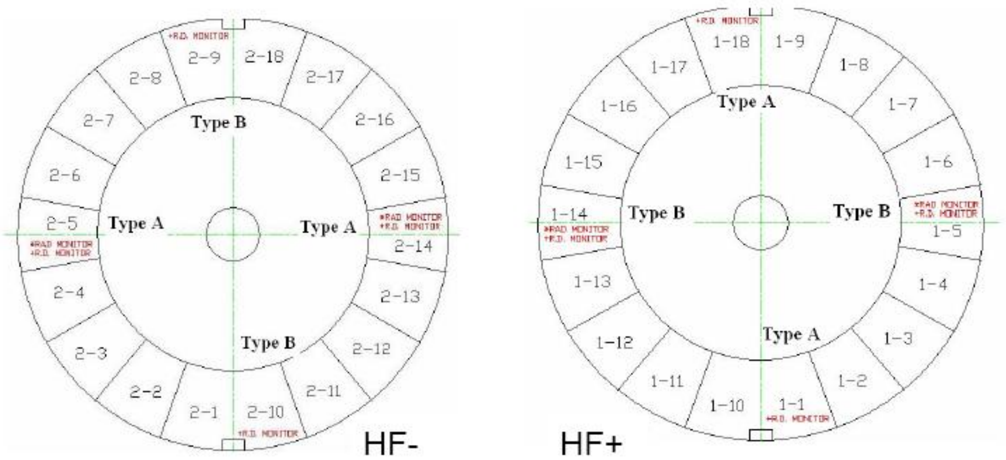

Figure 2.5. HF Raddam fibers installation.

We introduced the system in this section, results of the test of the system will be given in analysis chapter.

2.2. Beam Test of CASTOR Prototype IV

The beam test of prototype IV was performed in the H2 line at CERN Super Proton Synchrotron (*SPS*) during the two weeks in July-Aug 2008. Before the beam test the prototype was constructed at CERN and I took part during this construction. In the following part the details of the construction are given.

The production of CASTOR prototype IV consists of cutting, lapping and polishing steps of the quartz and tungsten plates. All operation was performed on the machines located in the CMS-ECAL Crystal Laboratory. For electromagnetic (EM) and hadronic (HAD) sections, with a total of 28 readout –units (*RUs*) (Figure 2.6.) were constructed with successive layers of tungsten (*W*) plates as absorber and fused silica quartz (*Q*) plates as active medium. The CASTOR Calorimeter has 224 (16×14) subdivision in total. The Cerenkov light produced by the passage of relativistic particles through the quartz medium, is collected in sections of 5 *W/Q* layers along the length of the calorimeter and focused by air-core light guides onto the PMTs. (CASTOR EDR, 2007)

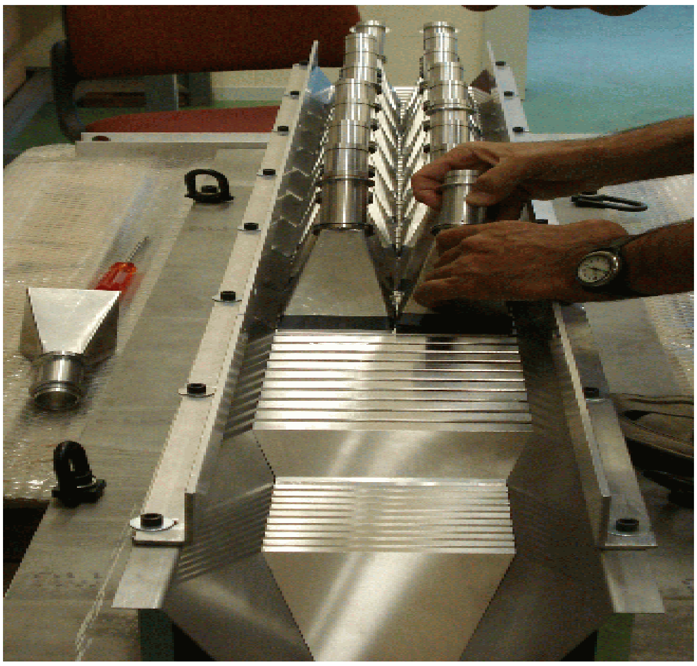

Figure 2.6. Assembly of light guides onto *W/Q* sampling units of prototype IV.

2.2.1. Tungsten-Quartz Plates

The calorimeter is constructed from layers of tungsten, containing 97% *W*, 1.3% *Fe* and 1.7% *Ni,* the density is 18.5 ±0.2 g/cm^3 . For the electromagnetic section, the *W*-plates have a thickness of 5 mm and the Q-plates 2 mm. For the hadronic, the *W*- and *Q*-plates have larger thicknesses of 10 mm and 4mm, respectively. The *W/Q*-plates are inclined 45^0 with respect to the direction of the impinging particles, in order to maximize the Cerenkov light output in the quartz. Each individual layer of *W/Q*-plates is called a sampling unit (*SU*). Figure 2.7. shows one example to tungsten plates, and Figure 2.8. shows one example of quartz plates. (CASTOR EDR, 2007)

Figure 2.7. Example of a tungsten plate used for the assembly of prototype IV.

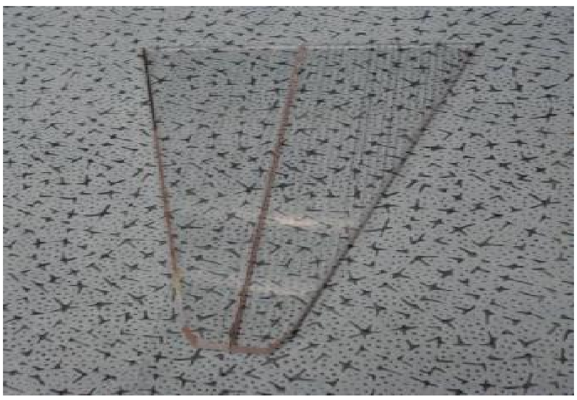

Figure 2.8. Example of a quartz plate used for the assembly of prototype IV.

2.2.2. Air-core Light Guides

The Cerenkov light emitted by the quartz plates is collected and transmitted to light-reading devices through air-core light-guides. The efficiency of light transmission and its dependence on the light-source position are crucial parameters, which characterize the light guide and significantly affect the performance of the calorimeter. Figure 2.9. shows HAD light guides. HAD and EM light guides differ from each other. The light guide on the EM section is shorter than the HAD one in length. (CASTOR EDR, 2007)

Figure 2.9. Air-core light guide designed for prototype IV and reflecting foil covering inside.

2.2.3. Readout Units (Photomultipliers) and Bases

The air core light guides transmit the Cherenkov light to the light-reading devices. For the light collection two different types of PMTs were used. One of them is the Hamamatsu R5380Q and while another one is a radiation-hard multi-mesh FEU-187 from RIE St. Petersburg, with cathode area ~2 cm^2. (Figure 2.10.). (CASTOR EDR, 2007)

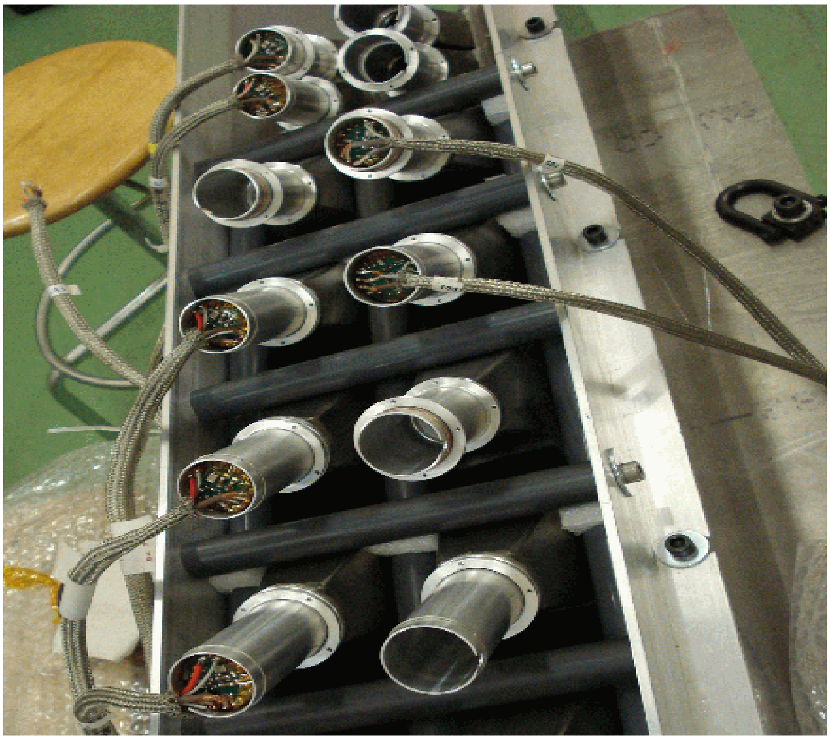

Figure 2.10. CASTOR PMTs on top of the light guides and bases used in the 2008 beam tests.

After completion the detector was taken to the H2 beam line of the SPS at CERN for the beam test. Detail of the setup and results are given in the analysis chapter.

3 . ANALYSIS AND RESULTS

In this section, the analysis results of online Raddam monitoring system of HF and analysis results of beam test of CASTOR will be presented. Before this beam test, there were several beam tests which aimed to study the performance of the three prototypes (I, II and III) of CASTOR calorimeter (CASTOR EDR, 2007) . All tests were conducted at the H2 CERN/SPS beam line using different types of particles with different energies. In this study the analysis results mainly focus on the energy response of EM section of the CASTOR prototype IV.

3.1. The HF Radiation Damage Online Monitoring (Raddam) System

3.1.1. Data Taking (2008-2009)

In 2008-2009, a test was performed with cosmic rays involving almost all of the sub-detectors of CMS which were working properly. During this global data taking activities Forward Hadron Calorimeter system recorded data during orbit gap sending laser pulses. This was the first opportunity to check the HF Raddam system in CMS global running conditions.

At the same time, regular local maintenance runs were taken daily using laser signals. This data is also used to analyze the Raddam system. In this work the comparison between the global and local data collected at HF Raddam system is presented.

3.1.2. Local Runs with Time Information (HCAL Timing)

There are two methods of raddam analysis by using time information and without time information. Timing, signal events are expected to occur within a known , fixed narrow phase window with respect to the LHC clock. This is used to reject background events that are "out-of-time" and for monitoring the phase stability of the readout. Precise time reconstruction of signals is achieved largely because each event appears as a pulse that stretches over several time sample intervals (a time sample is 25 ns, the interval between bunch crossings). This pulse shape is determined by characteristics of the sub-detector; which include time constants associated with the scintillator material, with the photo-detector, and with the readout electronics. The electronics introduce an additional complication as the scintillation pulse is not sampled, but rather integrated over each time sample.

The amount of time it takes the laser to fire fluctuates from pulse to pulse; this is known as "laser jitter". Using a Time-to-Digital-Converter (TDC), we measure the time the signal was sent to fire the laser (the "trigger") and the time the laser actually fired (the "opt sync" signal, created using a PIN diode located near the laser's aperture). (Particle Data Group). The effect of this jitter is shown in Figure 3.1. which shows the difference in time between the opt sync and trigger signals for multiple laser pulses. In the local run with timing information (TDC) one knows the two main time slice where the Raddam signal appears in the ADC content of time slices $TS(i)$ and $TS(i+1)$. The plot of $TS(i)/TS(i+1)$ versus the event time presents a plateau where the laser jitter is lower than 10 ns giving the stable ratio of Raddam signal,

$$R = S1/S2 = TS(i)/TS(i+1). \qquad (3.1.)$$

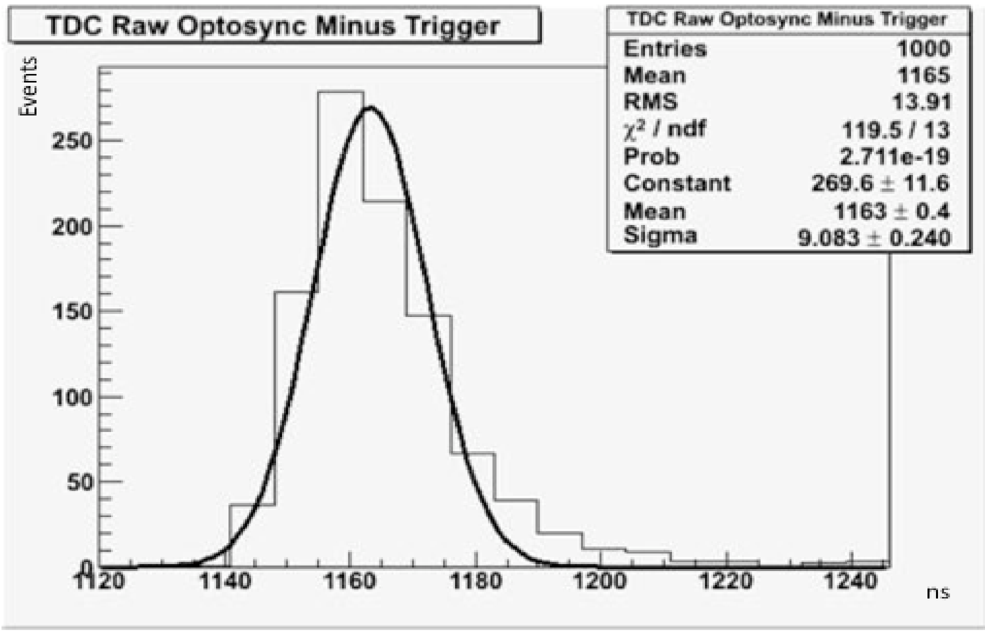

Fig 3.1. Time Digital Converter TDC information for a local run.

3.1.2.1. HF Pulse Shape from Laser Response

An ultraviolet (UV) nitrogen laser provides light with a wavelength of 337 nm that excites the HCAL's scintillators, thus emulating a hadron's traversal. The laser calibration system distributes the light to various HCAL readouts using a collection of fiber optic cables. The light is directed into multiple regions of the detector with a selection device; individual elements of the detector cannot be singly addressed given the substantial amount of channels involved. The laser pulse has a known time structure and its intensity is varied via filters. These two features combine to provide a versatile calibration and monitoring system. To maximize the amount of light transmitted, the placement of all optical components must be accurate to 10 µm. Because small vibrations or tensions in the table are detrimental, the laser calibration system is constructed on an optical breadboard. The breadboard dampens vibrations and prevents warping under heavy mechanical loads.

The laser emits pulses where the pulse-to-pulse energy variations are specified to be 4% and the beam-spot size is originally 8×8 mm^2 . In order to control the intensity of the pulse, the laser beam is incident upon two continuously varying neutral density (ND) filter wheels. The filter wheels contain an ND coating, which attenuates the light passing through it. For a single wheel, the attenuation across the beam-spot is not uniform due to the large beam-spot size. This becomes more significant since the beam-spot shifts slightly from pulse to pulse. Therefore, two filter wheels – facing in opposite directions are used; when rotated in anti-correlation, the beam-spot is uniformly attenuated. Each filter wheel is controlled by a rotary stepping motor and is specified to be linear in optical density as the wheel is changed by equal angles: $\log_{10} [S/S_0]$, where S (S_0) is the optical density at an arbitrary (reference) position. The level of attenuation increases with the rotational angle.

Subsequently, the beam passes through a focusing lens with a focal length of 20 cm. This focuses the beam-spot down to several hundred micrometers in diameter to better match the size of the quartz fibers that ultimately route the light to the HCAL. The beam is then incident upon the first of two beam samplers, each picking off 5% of the incoming pulse energy. The beam samplers are held by mirror gimbals, which allow the angle of incidence to be controlled. Two samplers are used in order to obtain various laser beams with diverse intensities; hence, the laser light is sampled regardless of attenuation setting. The first sampler reflect two beams to a second sampler and transmits one beam to the fiber harness. The fiber harness, controlled with a linear stepping motor, is moved such that the beam enters one of the thirty possible quartz fibers held within (these fibers ultimately route the light to the HCAL scintillator tiles). Each reflected beam incident upon the second sampler creates two additional reflected beams and one transmitted beam. These reflected/transmitted beams are fed into quartz fibers that route the light to Pin diodes. The Pin diodes allow us to measure the intensity of the light independent of the HCAL detector-via an oscilloscope or data acquisition system. The signal produced by a UV flash in the scintillator is similar to the signal induced by a traversing particle; therefore, can be mimic the time-of-flight of a particle from the interaction point by controlling the lengths of the fibers entering each tile. This arrangement allows the timing of all HCAL channels to be synchronized/monitored and allows for a performance check of the entire optical route from scintillator to electronics. Moreover, it provides an important technique to check for defective channels and to track possible degradation of signal amplification due to the component aging, temperature dependence, and radiation damage.

The laser delivers 10 pulses per second. More than 90% of the charge is within a single LHC bunch crossing (25 ns). Signal is mainly 90% in 25 ns. This corresponds to one time slice when the peak of the signal is centered in this time slice. (CMS Physics TDR, 2007).

With my present methods of analysis using the laser data is shown Figure 3.2.

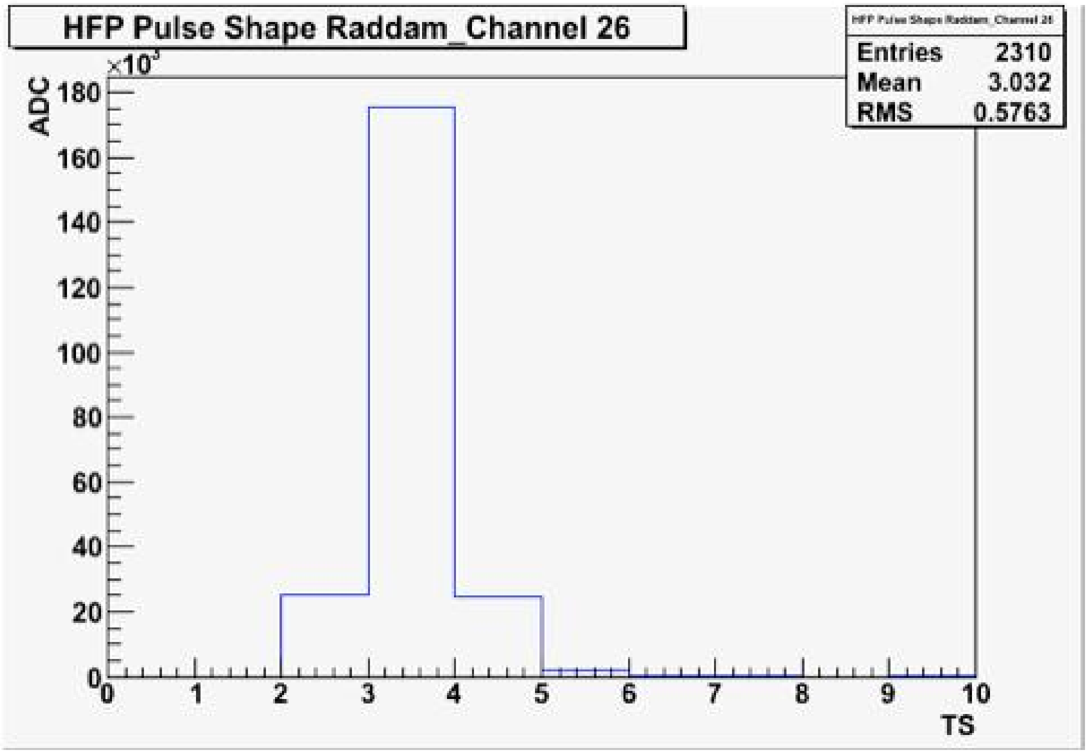

Figure 3.2. HF Laser Pulse Shapes for one channel.

3.1.2.2. Ratio of Raddam Channel in Local Runs

Until first pp collisions from LHC are recorded, cosmic-ray events were the most powerful source of data for CMS. With cosmic-ray muons, one can calibrate and test Hadron Calorimeter (HCAL) components, thus improving our understanding of the detector. The purpose of SATOCRICH project (Special Assignment to Observe Cosmic Rays in CMS HCAL) was to collect and analyze the first sample of cosmic-ray events for CMS HCAL. Two reflected Raddam signals separated by 25 ns are read out coming in two adjacent time slices (TS) when the laser timing and the read out electronics are well matched. The transparency of one fiber is obtained from the ratio of ADC counts (or *fC*) in these two adjacent TS. The Raddam system is based on the continuous measurement of the ratios of these 2 signals (*S*1/*S*2) for example see in Figure 3.14. Since the end of the HF Raddam fiber is closer to the interaction point, the signal reflected from the end of it (*S*2) decreases with the radiation.

The pulse shape of Raddam fiber signal in ADC counts can be seen in Figure 3.3. Since we don't know exactly the charge distributions in each TS due to the laser jitter and imperfections in timing, we obtained the ratio of the first reflection (*S*1) over the second reflection (*S*2), histogramming the ratios as a function of phase that is defined as time difference between TTC and Laser trigger (we refer it as a time information later in this text) in Figure 3.4. Then the plateau part of this ratio (*S*1/*S*2) was fitted to a horizontal line as can be seen in the Figure 3.4.

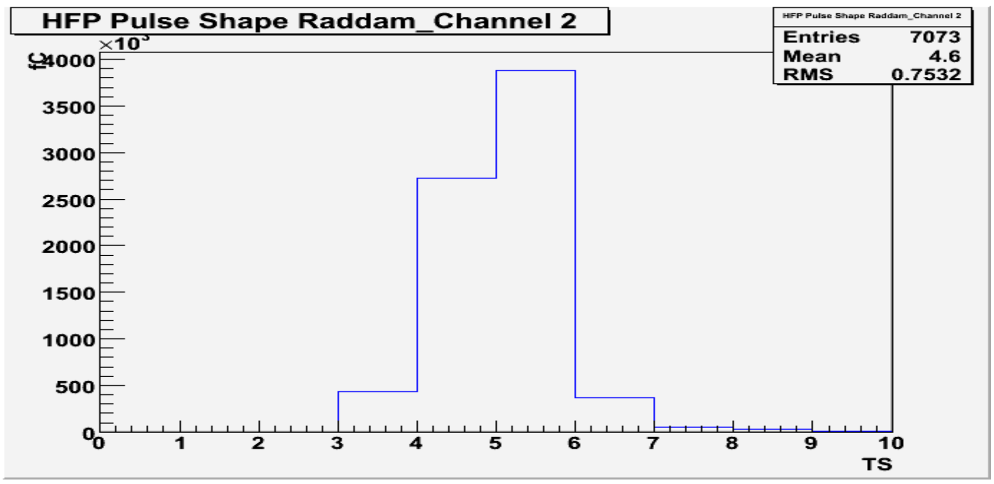

Figure 3.3 Pulse shape from HFP for one Raddam channel.

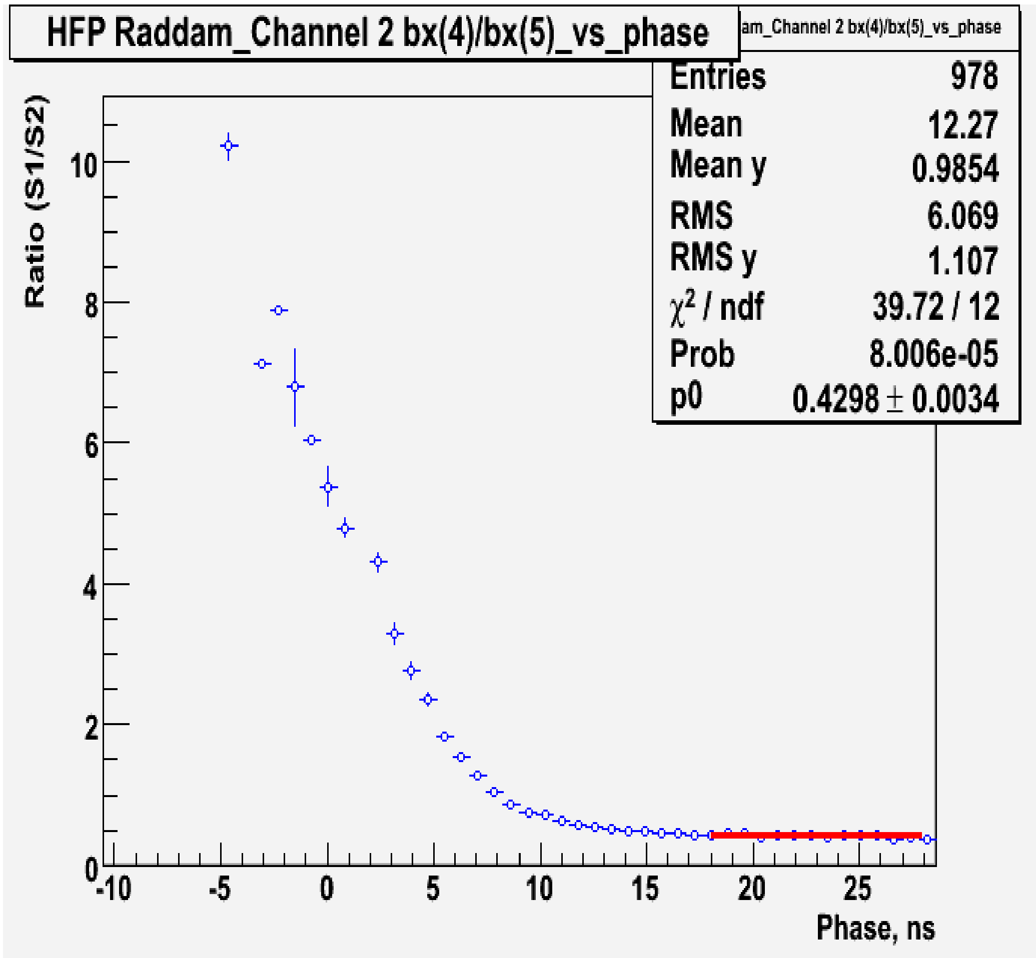

Figure 3.4. Ratio of the two signals within 25 ns using time information.

Frequently the signal is contained in two time slices. But in the local runs there are a lot of events, which are out of the two time slices due to laser jitter as seen in the Figure 3.4. During this analysis this ratio is separated into three regions (see Figure 3.5). For each run we select events which is in the second region which means that signal is completely with in two time slices and check whether for all other channels signal is in two time slices. And we see that in all channels signal contained in two time slices. In addition, we excluded all events if 90% of the signal is not contained in two time slices according to equation (3.1).

$$[TS(i\text{-}1)+TS(i+2)]/[TS(i)+TS(i+1)]<0.10 \qquad (3.2)$$

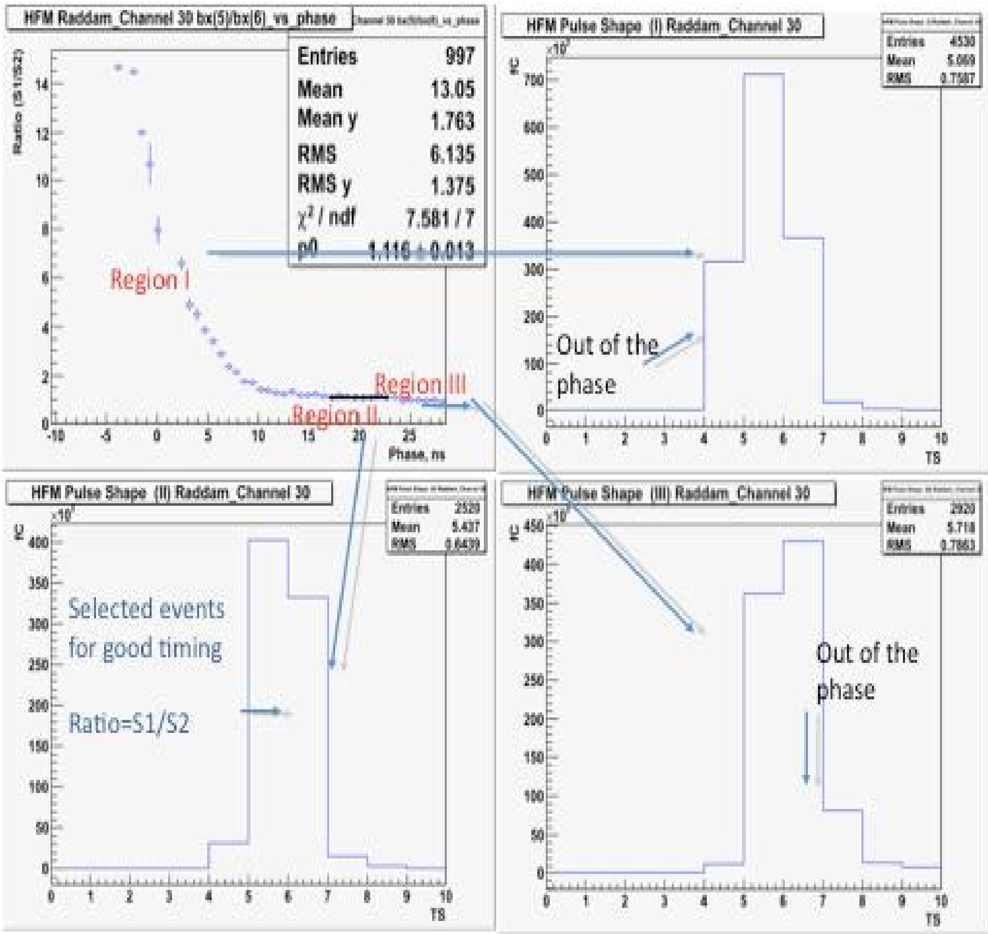

Figure 3.5. Ratio of the two signals divided into three regions for the local run .

After we selected events, which are in the second region, we compare the ratio of the two signals in two different ways: with and without using the time information. If we use the time information we get better results as can be seen from Figure 3.6. Also event selection described above gives almost the same results. This event selection method was applied to all HF Raddam channels.

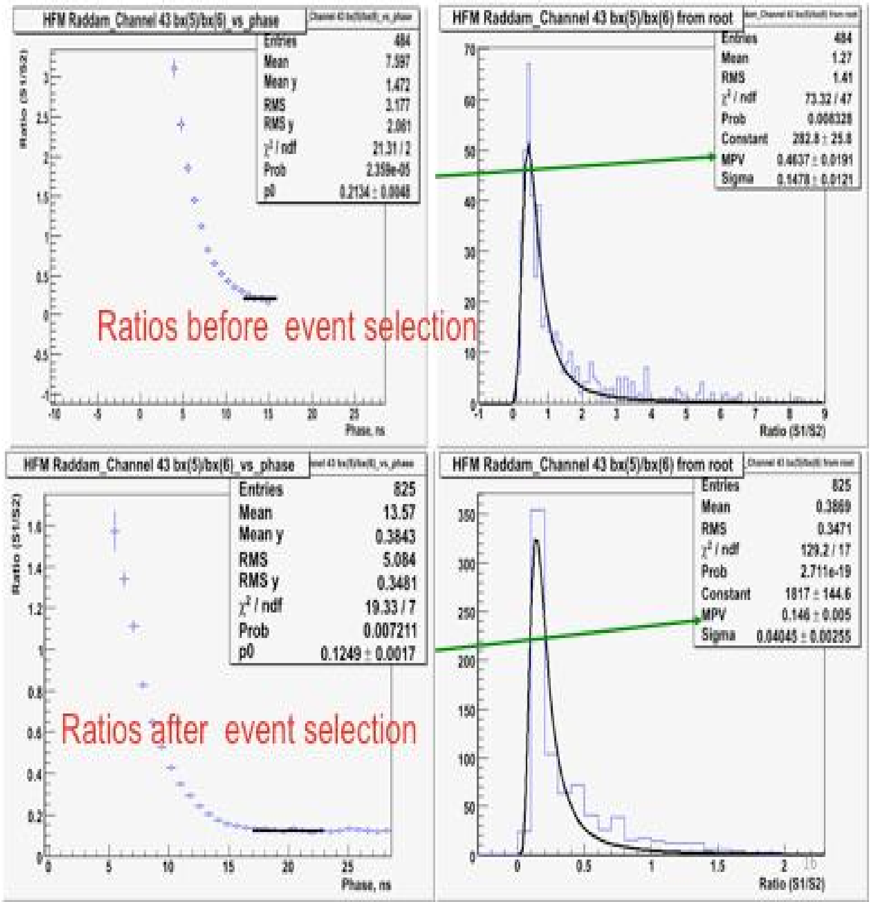

Figure 3.6. Top plot on the left shows the ratio using time information and top-right the ratio without it but both are without any event selection. Bottom left shows the ratio with time information and with event selection while in bottom right only event selection is applied.

3.1.3. Global Runs Without Time Information

The LHC frequency of 40.08 MHz corresponds to a 24.95 ns period. One LHC orbit consists of 3564 periods. They are often called “bunches” although some of them do not contain protons. The proton bunches are grouped in 39 trains, 72 bunches each. The structure of gaps between them can be used for the absolute synchronization. The main gap has a length of 3 µs (119 missing bunches.

At the LHC start the machine will operate with proton bunches 75 ns apart. This operation condition is well suited to establish the trigger and readout synchronization.

At LHC, the laser pulses are injected during 3.17 μs gaps foreseen every 88.924 μs in the LHC beam structure. Running the laser source at 10 Hz means injecting laser pulses in 0.1% of the available gaps.). (CMS Physics TDR, 2007).

Global Raddam runs, which were taken without the time information, were investigated using “Landau-Moyal” method. We applied event selection which is explained in previous part to this data to exclude problematic events due laser jitter or some electronic noise.

During the LHC shutdown CMS experiment was taking events using cosmic rays. During orbit gap also Raddam runs were taken. This kind of runs were referred as global runs and during this run timing information is not available due to the HCAL electronic structure.

The distribution of $R = TS\ (i)\ /\ TS\ (i{+}1)$ is fitted to Landau-Moyal type and this fit gives the most probable value for the ratio R. In Figure 3.7. on the left plot signal distribution is shown as a function of the time slices for one event and for one channel while on the right plot, ratios are given for all events and for all runs and also Landau-Moyal fit is shown in the same plot. This result is obtained without using the time information but using the event selection.

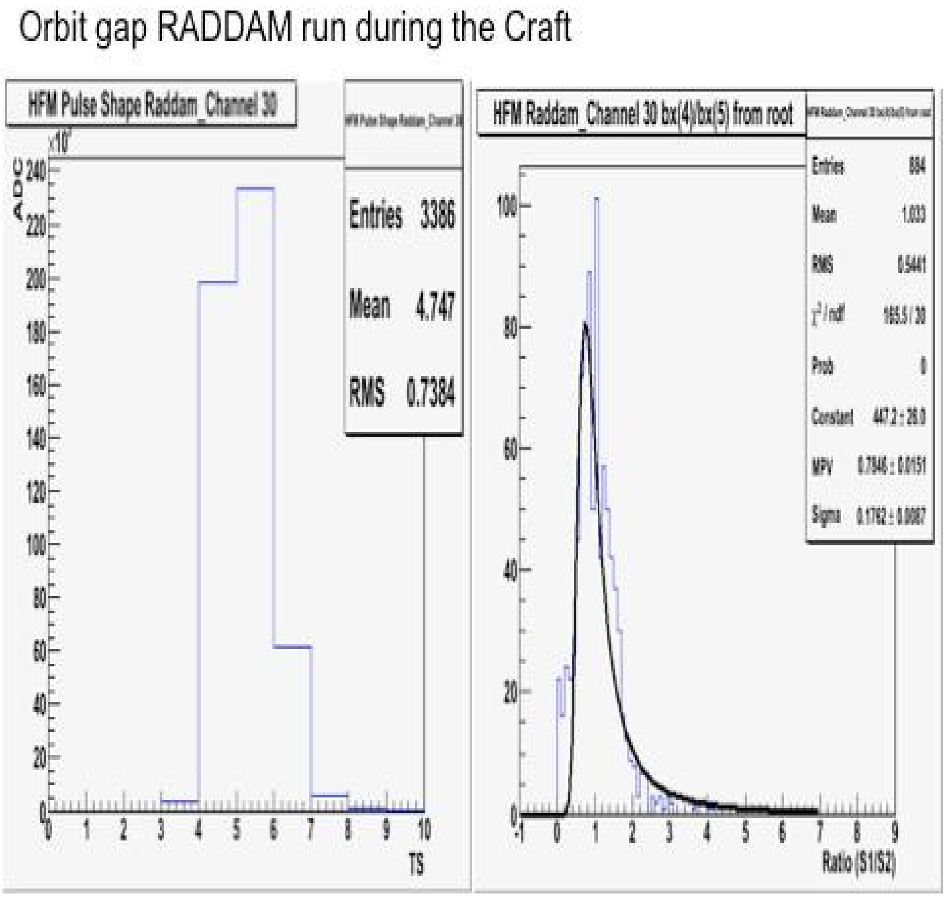

Figure 3.7. HF Raddam pulse shape which is taken during the orbit gap is shown on the left plot, the ratios of two time slices with fit to the Landau –Moyal is shown on the right plot.

3.1.4. Comparison of the results of Local and Global runs for all channels

In this section, comparison of analysis results of Local and Global runs will be given. After applying all event selection criteria, acceptable ratios were obtained as is shown in the Figure 3.8.

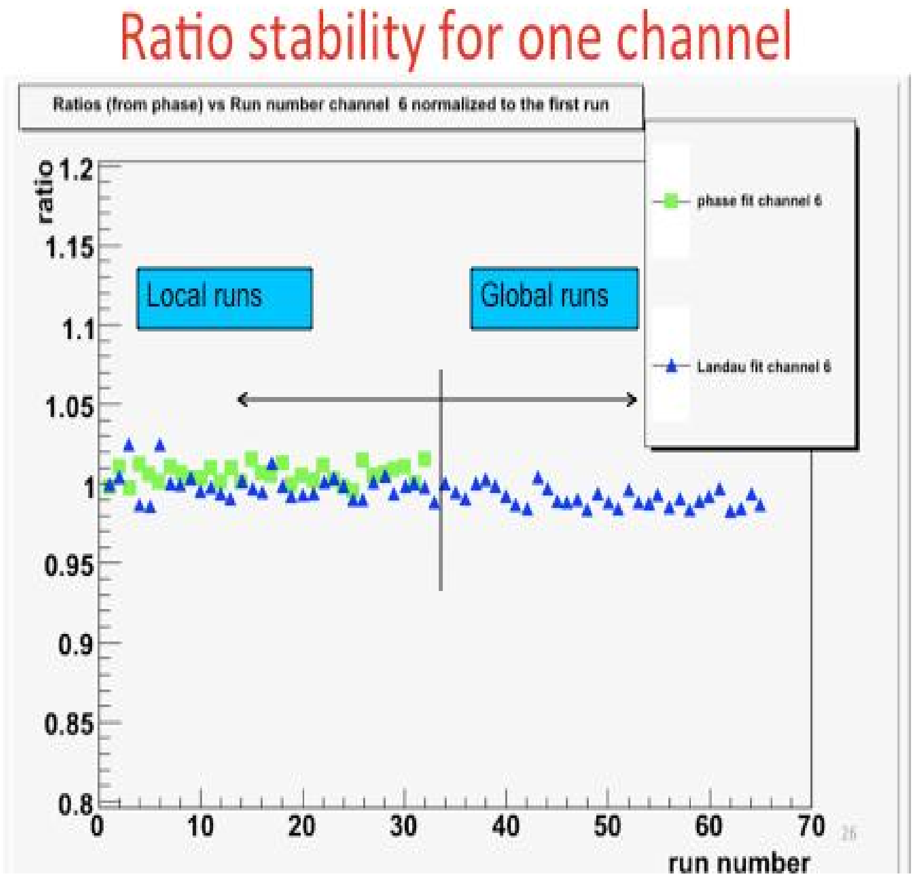

Figure 3.8. Ratio Stability for one channel

About 90% of Raddam signals work properly with the Landau method in the abort gap. Results are shown for 40 runs and 56 Raddam channels with phase method in Figure 3.9. with Landau method in Figure 3.10. As can be seen the difference between the two methods (Phase and Landau) is less than % 0.1.

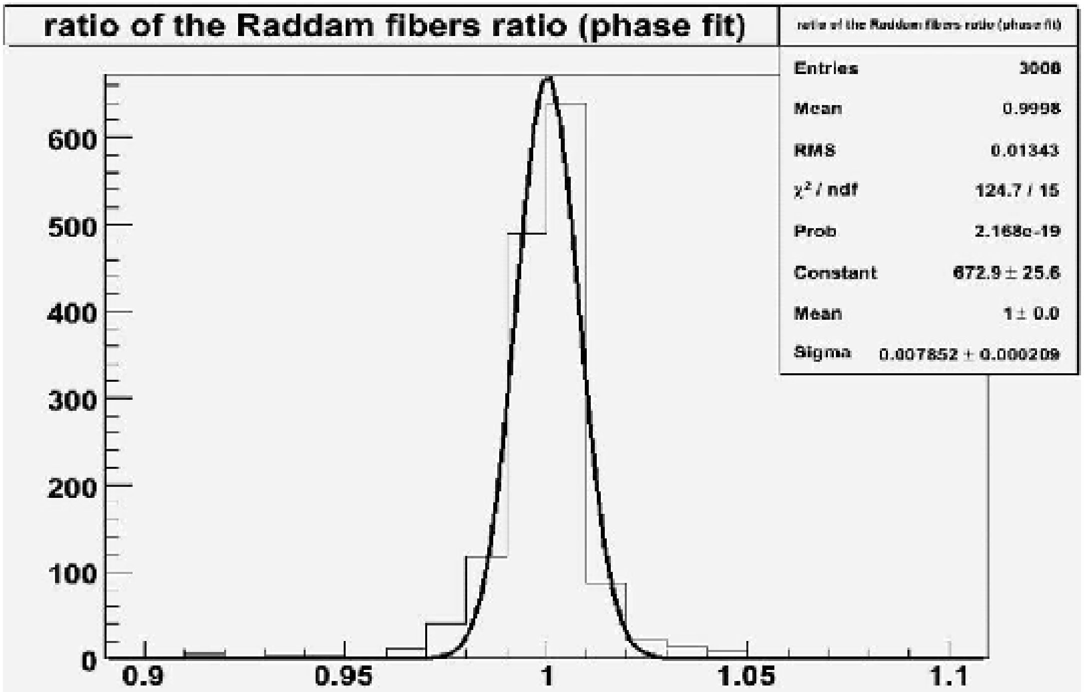

Figure 3.9. Ratios with time information.

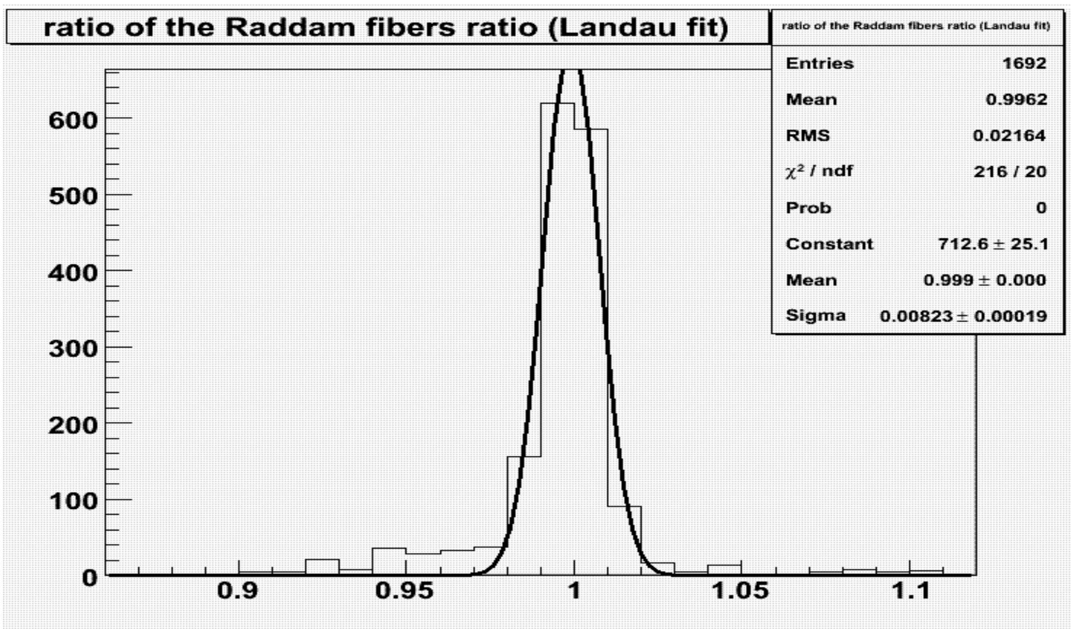

Figure 3.10. Ratios without time information.

3.2. Beam Test 2008 of CASTOR Prototype-IV

The beam test of final prototype was performed in the H2 line at CERN Super Proton Synchrotron (SPS). Electron, hadron, and muon beams of several energies were used. The energy responses (linearity and resolution) of the electromagnetic and hadronic sections were obtained through energy scans with: 10-200 GeV electrons, 20-350 GeV pions as well as 50-150 GeV muons. A schematic description of the H2 beam line of the SPS at CERN is shown in Figure 3.11. Information from wire chambers which are located at upstream of the prototype IV was used for finding the precise location of particles where they hit the calorimeter.

The prototype IV consisted of a full-length octant, containing the electromagnetic (EM) and hadronic (HAD) sections, with a total of 28 readout-units (RUs) is shown in Figure 3.12.

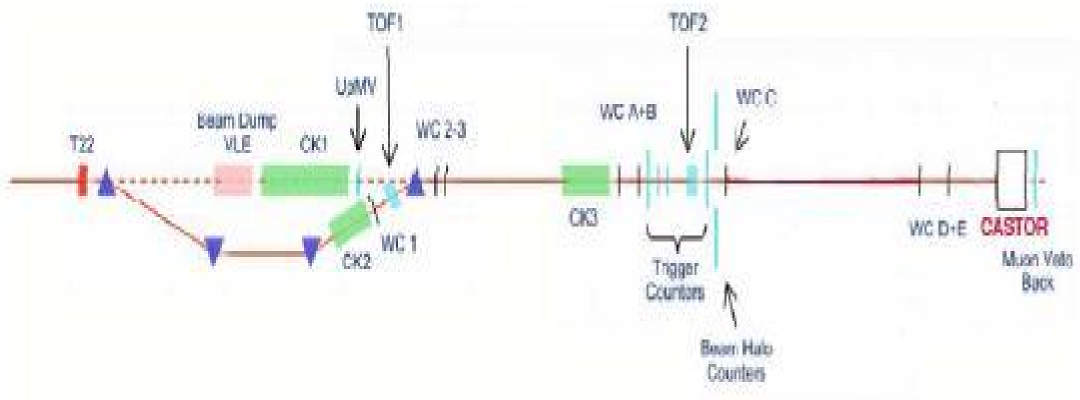

Figure 3.11. Schematic figure of the H2 beam line of the SPS at CERN (CASTOR EDR.).

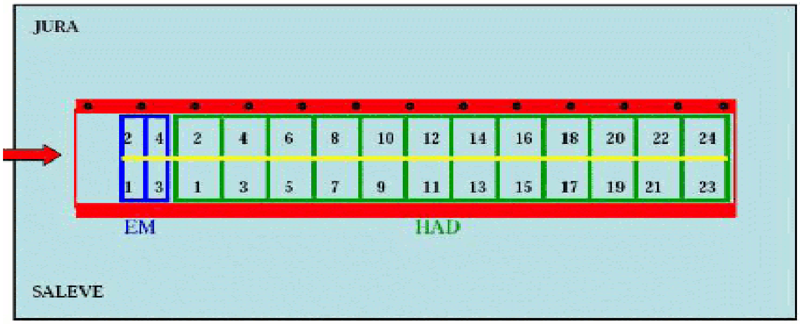

Figure 3.12. Schematic drawing of the 28 readout units (RUs) of CASTOR prototype IV.

The CASTOR calorimeter has two semi-octants which is constructed at 45^0 which is the optimum angle for collection of Cerenkov light as shown Figure 3.13. Each semi-octant consist of electromagnetic and hadronic parts.

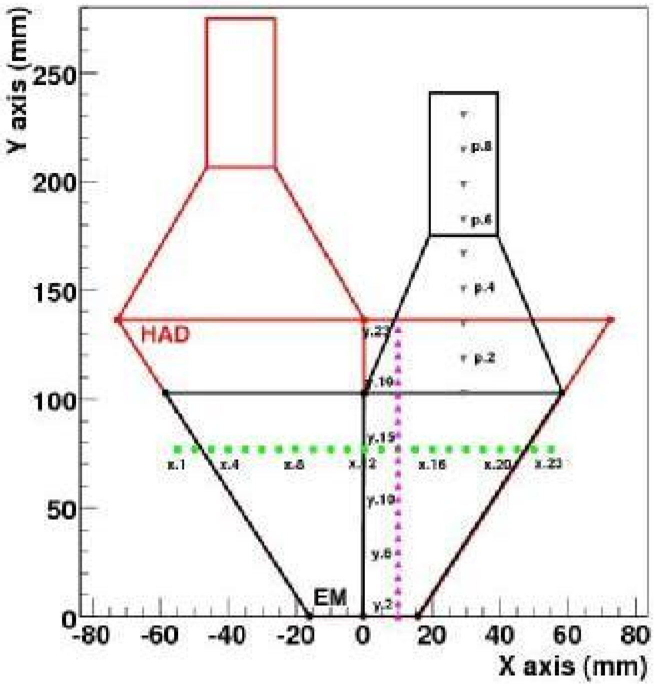

Figure 3.13. Production of the front face of the EM (black lines) and HAD (red lines) sections onto a 45° vertical plane (Aslanoglu et al., 2008).

3.2.1. Electron Beam

Electron beams of energy 10-200 GeV were used to test the energy linearity and resolution of the EM section of the prototype. For all studies, a central point in the calorimeter was selected applying a 1 cm x 1 cm cut on the spatial profile of the beam as measured by the upstream wire chambers (Fig. 3.14.).

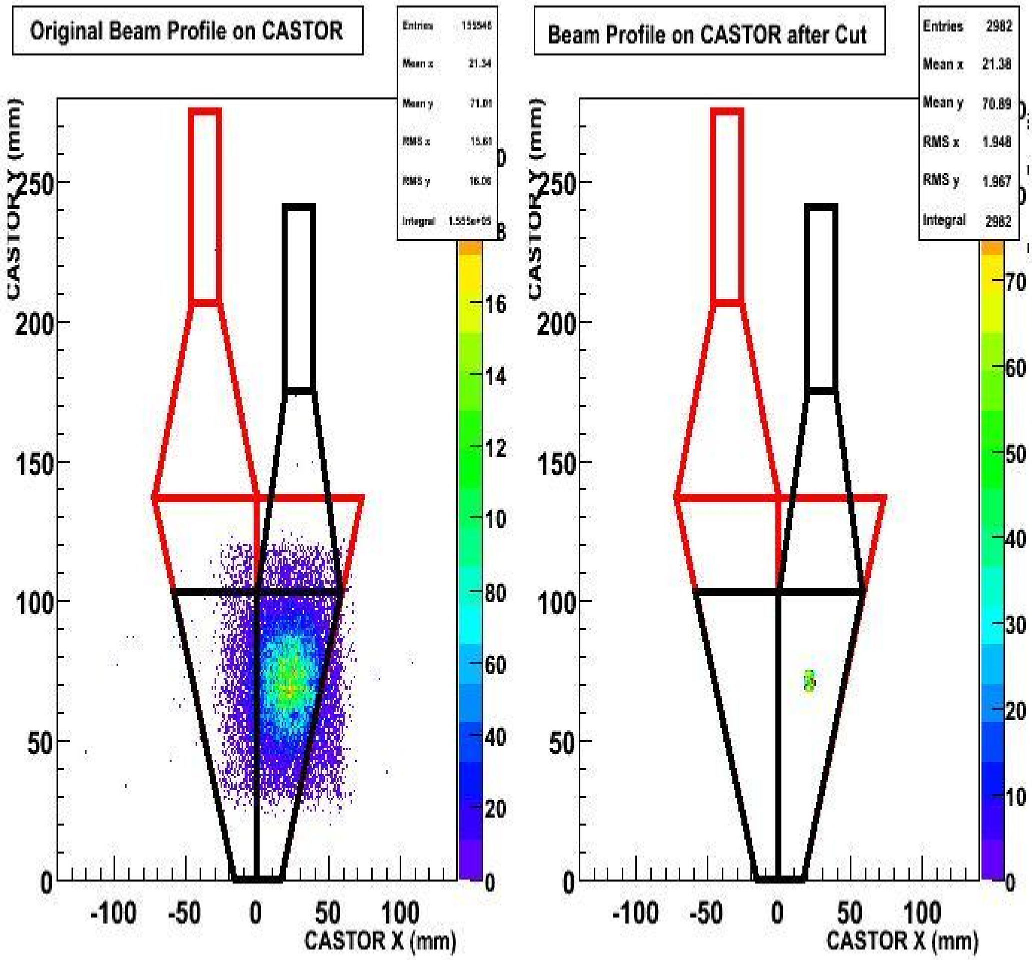

Figure 3.14. Beam profile projected onto the front face of the calorimeter using the hits distribution from the WC-D, before (left) and after (right) a spatial cut (Aslanoglu et al., 2008).

3.2.2. Energy Scan With Electrons

Electron beams of energies 10-200 GeV were used to study the energy response linearity and resolution. These runs are shown in Table 3.1.

Table 3.1. Electron signals from test beam 2008 in the CASTOR.

Run number	Energy (GeV)	Table X	Table Y
48514	10	-20	-3
48582	20	-20	-3
48593	50	-20	-3
48649	120	-20	-3
48650	150	-20	-3
48655	200	-20	-3

Scintillator-wire chamber hits are shown in Figure 3.15. for one of the electron runs which contain around few thousands events. WCA is not used for analysis since it was not working properly during test beam. Also there are some missing events in WCD data. Although WCA is the closest wire chamber to prototype, chamber E and D were used since WCA was not functioning.

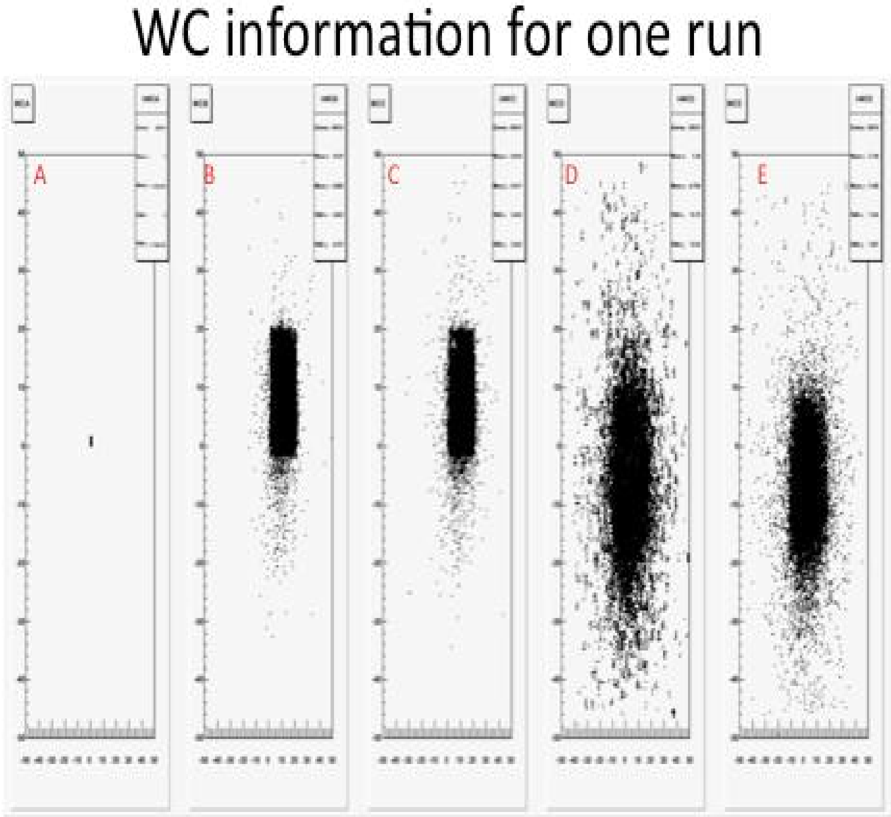

Figure 3.15. Wire chamber information for electron signal, (run number, 48514) .

To be able to select single hits scintillator cuts were applied during analysis of the test beam data. The trigger counters are polystyrene scintillators of 1 cm thickness, therefore electrons and pions behave as Minimum Ionizing Particles (MIP). The peak position and width of an *MIP* was fitted by a Gaussian distribution and only events with ADC counts within 3 sigma were selected as single particle events as shown in Figure 3.16.

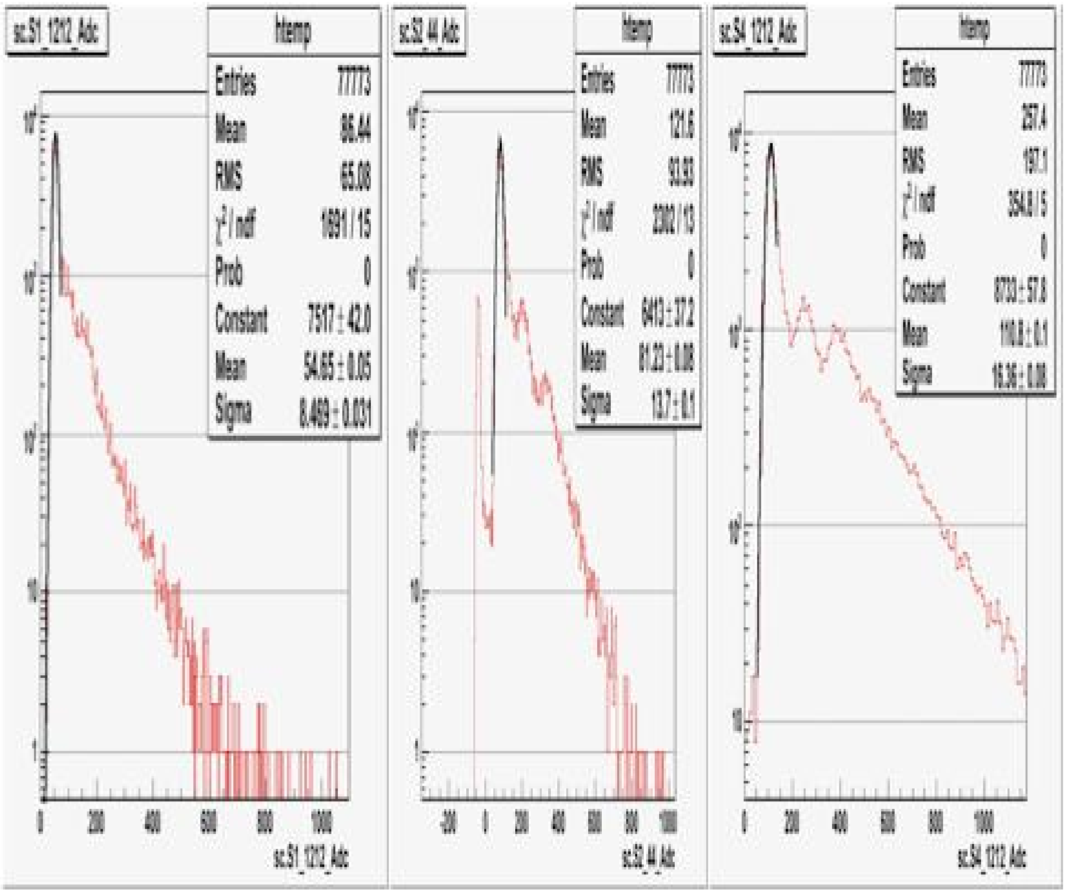

Figure 3.16. ADC distribution of scintillator counters SC1, SC2 and SC4.

There are muon counter to veto the muons contamination in the beam as can be seen from Figure 3.12. In Figure 3.17 ADC distribution of this counter is shown. Second bump corresponds to muons. A Gaussian was fitted to this bump and all signal within 3 sigma considered as muons and rejected.

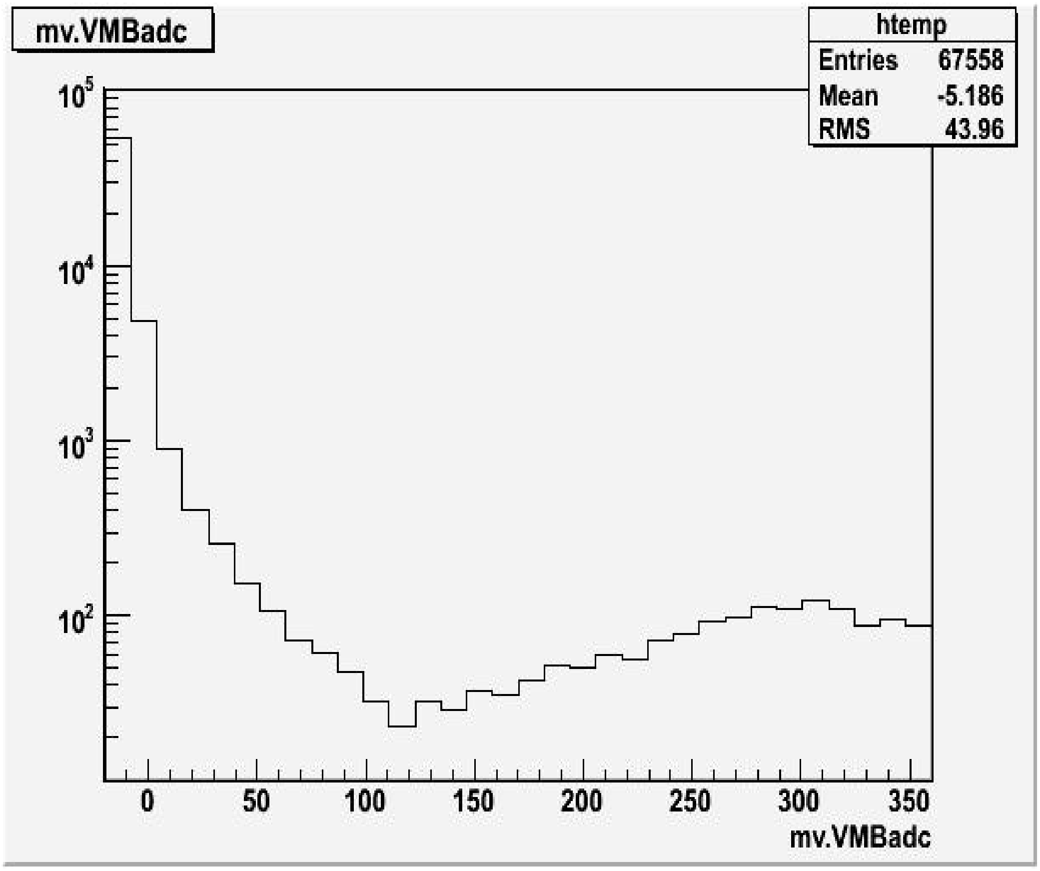

Figure 3.17. ADC distribution of muon veto counter for 120 GeV electron run.

After applying above cuts the remaining events were plotted as a histogram as is shown in Fugure 3.18. Horizontal axis is ADC counts for each event while the vertical axis is number of events at this count. This corresponds to the energy distribution since ADC count is a linear function of energy. This energy distribution is fitted using a Gaussian function. The mean of each energy distribution was plotted as a function of beam energy and fitted using parameterization given by equation 3.2.

$$\text{Average signal amplitude in ADC count} = a + b\times E \quad (3.3.)$$

where the energy E is in GeV.

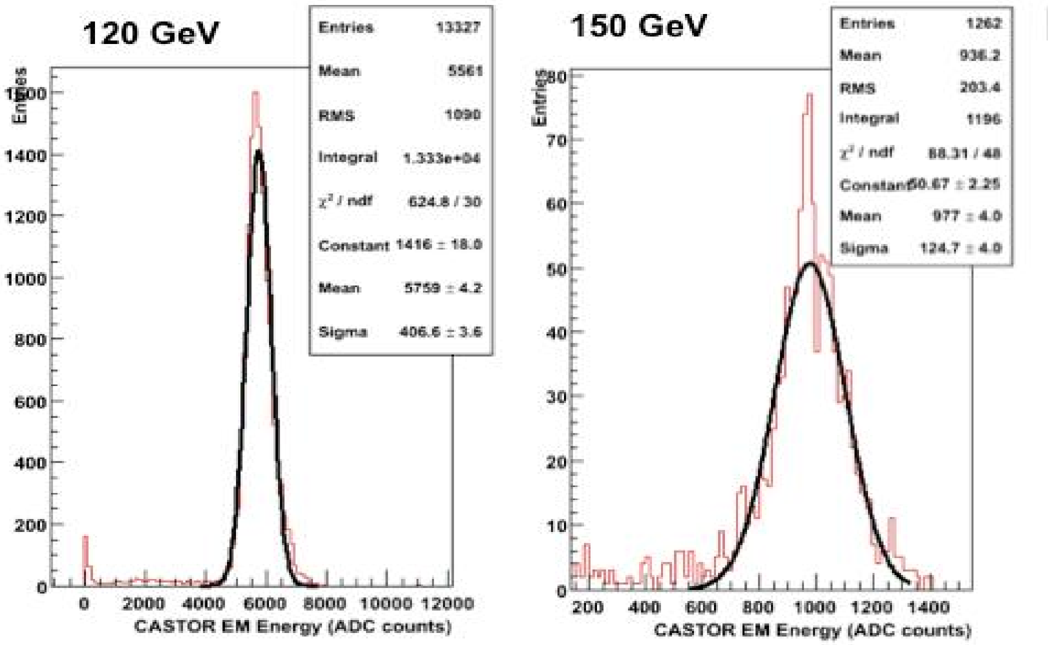

Figure 3.18. Total energy distribution for various electron energies.

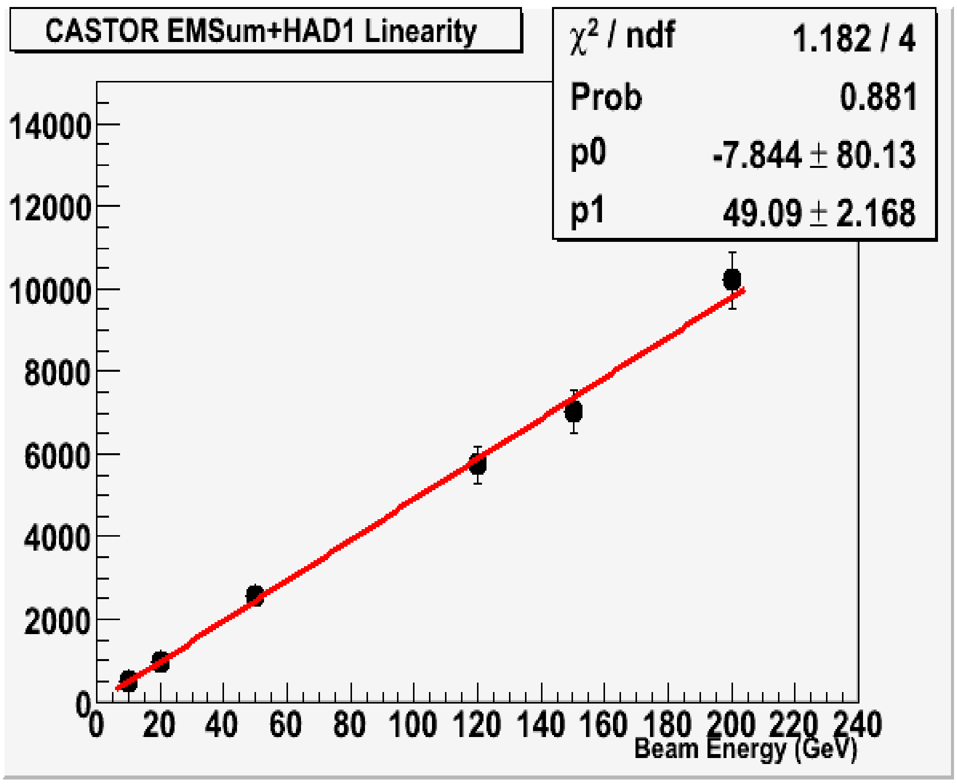

Figure 3.19. Energy linearity of CASTOR Prototype IV.

As can be seen from the Figure 3.19. calorimeter response is linear as a function of increasing beam energy.

3.2.3. Energy Resolution

The relative energy resolution of the calorimeter had been studied by plotting the normalized width of the Gaussian signal amplitudes, *σ/E,* with respect to the incident beam electron energy, *E*(GeV) and fitting the data points with the two functional forms (Aslanoglou et al., 2008):

$$\frac{s}{E} = p_0 + \frac{p_1}{\sqrt{E}} \qquad (3.4.)$$

$$\frac{s}{E} = p_0 \oplus \frac{p_1}{\sqrt{E}} + \frac{p_2}{E} \qquad (3.5.)$$

Figures 3.20. and 3.21. show the measured energy resolution for the Hamamatsu PMTs. The measured stochastic term is 68-85 %, whereas the constant term is around 3-7%.

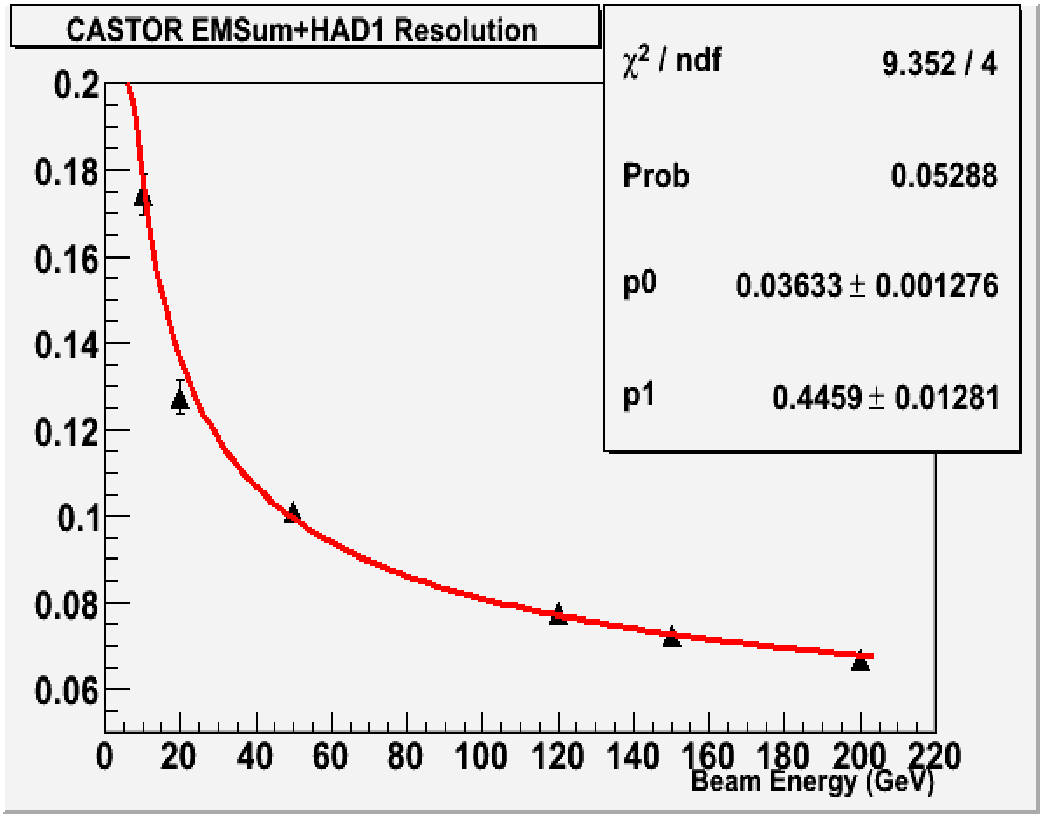

Figure 3.20. Energy resolution of prototype IV, the data points are fitted the equation (3.3.) with two parameters.

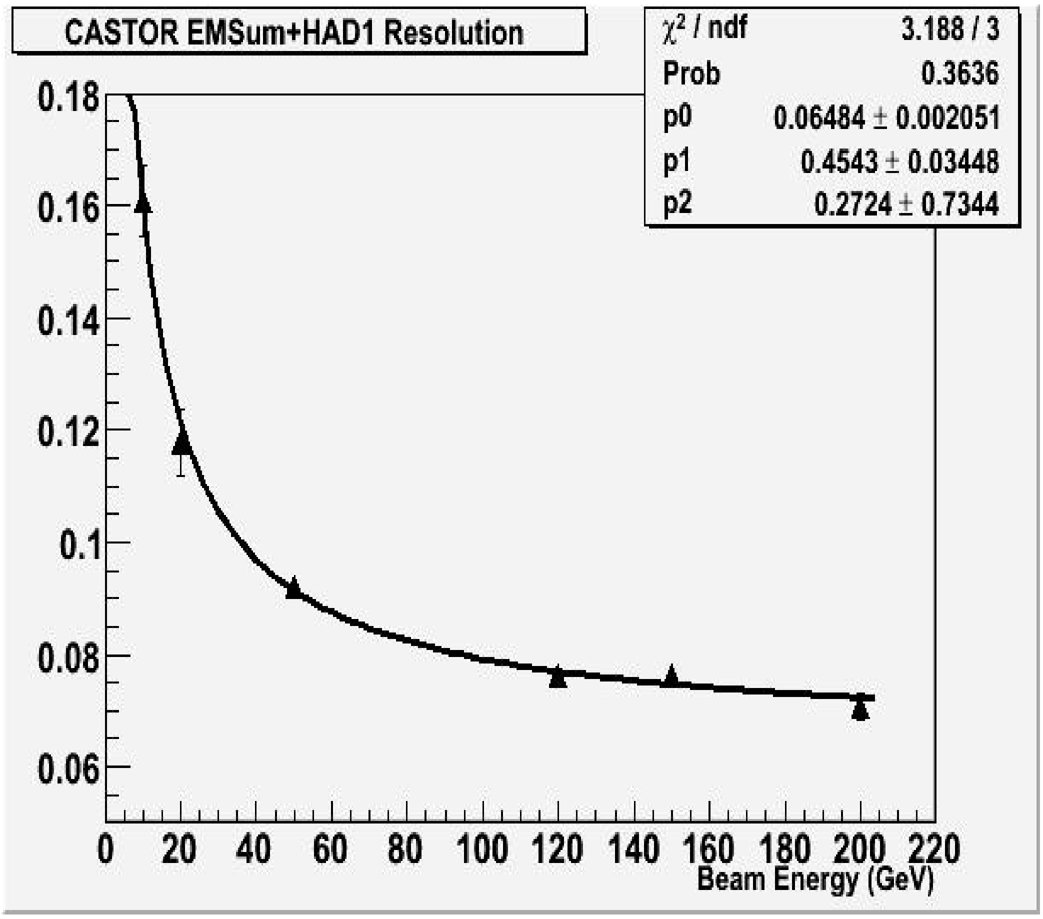

Figure 3.21. Energy resolution of prototype IV. The data points are fitted with equation (3.4.) using three parameters.

Figure 3.21. shows the plot of the relative resolution as a function of $E^{-1/2}$. It was found that the constant term p_0 was close to zero for all sectors. The measured stochastic term p_1 was in the range 24%-82%.

4. DISCUSSION AND CONCLUSION

The HF and CASTOR forward calorimeters will significantly enhance the pseudo rapidity range of the CMS experiment, providing useful energy measurements in the very forward region. With a broad physics program, both for proton-proton and lead-lead collisions, CASTOR and HF will contribute mainly to the study of exotic events in heavy-ions, low-*x* QCD and diffractive physics.

The analysis was performed using the CMSSW framework, as well as a stand-alone HCAL library. All Raddam data (global and local), which were taken during 2008-2009, were analyzed. In principle, we have two main raddam signals from the raddam system (shown in Figure 2.3.). The ratio $R = S_1 / S_2$ is related to the fiber transparency. But in the local and global runs there are a lot of events, which are not in the two time slices due to laser jitter as seen in the Figure 3.4. During this analysis, this ratio is separated into three regions (see Figure 3.5). For each run we selected events which is in the second region, which means that signal is completely within two time slices and check whether for all the other channels signal is in two time slices. As can be seen from in Figure 3.6. in the signal was contained in two time slices in all channels after event selection method was applied.

Two different methods (with and without time information) give results which are in agreement. This can be seen from Figures 3.9. and 3.10. The obtained values are in agreement with a spread lower than ~%1 after applying the cuts explained in previous sections. This results show that we can obtains the ratios even if we do not have the time information.

The test beam results for CASTOR, which is presented in this thesis, focus on the EM section of the prototype, and include studies for the energy response. It is shown that the prototype exhibits good energy linearity, while the energy resolution is characterized by a stochastic term of (68-85)%, p_1, due to intrinsic shower photon statistics, and a constant term (4-6)%, p_0, related to imperfections of the calorimeter. The results are summarized in Table 4.1. For relatively high energies, above 200 GeV, the energy resolution of the calorimeter was found to be less than 8%.

Table 4.1. Energy resolution fit parameters.

Fit formula	p_0	*p1*	*p2*	x^2/ndf
(3.3)	0.047 ± 0.002	0.32 ± 0.01	-	7.65/4
(3.4)	0.064 ± 0.002	0.45 ± 0.034	~ 0.28±0.73	3.188/3

For the analysis, a spatial cut on the profile was applied, using the ADC information of the downstream wire chambers, as well as cuts in the hadronic channels of the prototype, which made possible the study of the pion contamination of the beam. It was found that considerable amount of muon contaminates the electron beam. After the cut on the beam profile, the electron peaks were found to be significantly improved and well fitted by Gaussian distributions. For the summation of the energy in multiple channels of the prototype, the inter-calibration constants were used. They were calculated from the muon peaks, which were clearly separated from the pedestal.

Finally, we can say, according to results of the analysis, CASTOR calorimeter was working properly.

REFERENCES

AFFOLDER, T., et al., for the CDF collaboration, "Charged jet evolution and the underlying event in proton-antiproton collisions at 1.8 TeV", Phys. Rev. D, Vol. 65, 09-2002

ANGELIS, A.L.S. and PANAGIOTOU, A.D., 1997, CASTOR: A dedicated detector for the detection of centauros and strangelets at the LHC J. Phys. G: Nucl. Part. Phys. 23 (1997) 2069–2080.

ARNEDO, M. and DIEHL, M., 2005, arXiv:hep-ph/0511047 (2005) ASAI, S., et al., Eur.Phys.J. C32S2 (2004) 19-54

ASLANOGLOU et al., 2006, First performance studies of a prototype for the CASTOR forward calorimeter at the CMS experiment, CMS-NOTE 2006-142.

ASLANOGLOU et al., 2007**,** Performance Studies of Prototype II for the CASTOR forward Calorimeter at the CMS Experiment, arXiv:0706.2641v2 [physics.ins-det].

ASLANOGLOU et al., 2008, Performance studies of the final prototype for the CASTOR forward calorimeter at the CMS experiment CMS NOTE 2008/- (in preparation)

BASEGMEZ et al., 2008, Performance studies of the prototype III of CASTOR forward calorimeter at the CMS experiment, Presented at the Poster Session of the Quark Matter 2008 Conference, Jaipur, India, CMS-CR 2008/039

CASTOR Engineering Design Report, (EDR) 2007, CERN, https://twiki.cern.ch/twiki/bin/view/CMS/CastorEDR

CMS Physics Technical Design Report, (TDR) 2006, Vol I, CERN

CMS Physics Technical Design Report, (TDR) 2007, Vol II, CERN

CANKOÇAK et al., 2007, Radiation-hardness measurements of high OH^- content quartz fibres irradiated with 24 GeV protons up to 1.25 Grad NIM CMS NOTE 2007/03

D’ENTERRIA, D., Low-x QCD with CMS at the LHC, 2007, European Physical Jurnal C Eur. Phys. J. C 49, 155–16 (2007) The European Physical Journal C DOI 10.1140/epjc/s10052-006-0078-5

D’ENTERRIA, D.Forward Physics at the LHC, 2007, XV Workshop on Deep-Inelastic Scattering and Related Topics talk, Munich

D’ENTERRIA, D., 2007, CASTOR Physics, Beam-Tests Results and Calibration, CASTOR Engineering Design Review talk, CERN

D' ENTERRIA, D., et al. and the CMS collaboration, 2007, J. Phys. G: Nucl. Part Phys. 34 (2007) 2307–2455

D' ENTERRIA, D., 2008, Forward physics at the LHC: QCD, electroweak &Higgs, QCD- School Les Houches talk, March 25th - Apr. 4th, 2008

D' ENTERRIA, D., 2006.Desing, Performance, and Calibration of CMS Forward Calorimeter Wedges, CMS NOTE 2006/044

DUMANOĞLU, et all., 2002, Radiation-hardness studies of high OH^- content quartz fibres irradiated with 500 MeV electrons NIM A 490 (2002) 444-455

FABJAN, C.W. and GIANOTTI, F., 2003, Calorimetry for Particle Physics, CERN- EP/2003-075, CERN

GLADYSZ-DZIADUS, E., for the CASTOR group, 2001, CASTOR: Centauro And Strange Object Research in nucleus-nucleus collisions at LHC, arXiv:hep- ex/0209008v2 G. Ruggiero *et al.*, *IEEE Trans. Nucl. Sci.* **52** (2005), pp. 1899–1902

HEAVY ION PHYSICS TDR, 2007 Addendum I, (ed) D’Enterria, D. On behalf of the CMS Collaboration

LEO, W.R., 1994.Techniques for Nuclear and Particle Physics Experiments, New York

MAVROMANOLAKIS, G., 2003. Quartz fiber calorimetry and calorimeters, Cambridge, UK

MUELLER A.H. and NAVALET, H., Nucl. Phys. B 282 (1987) 727

PANAGIOTOU,A.P.,2007, CASTOR EDR approval talk, CERN

PANAGIOTOU, A.D and KATSAS, P., 2006, Search for Strange Quark Matter with the CMS/CASTOR detector at the LHC, Nuclear Physics A10674 (2006)

PARTICLE DATA GROUP, The Review of Particle Physics, http://pdg.lbl.gov/ P.W. Higgs, Phys. Rev. Lett. 12 (1964) 132; idem, Phys. Rev. 145 (1966) 1156; F. Englert and R. Brout, Phys. Rev. Lett. 13 (1964) 321 G.S. Gurainik, C.R. Hagen and T.W. Kibble, Phys. Rev. Lett. 13 (1964) 585.

P.W. Anderson, Phys. Rev. 110 (1958) 827; ***ibid.*** 130 (1963) 439. Comptes Rendus Physique, Volume 8, Issue 9, November 2007, P.W.Higgs, Spontaneous symmetry breakdown without massless bosons, Phys. Rev. 145 (1966) 1156.

VIRDEE, T.S., 1998, Calorimetry. CMS Collaboration,CERN, Geneva, CMS Conference Report,CMS-CR, 1998/026.

WIGMANS, R., 2000. Calorimetry Energy Measurement in Particle Physics, Oxford University Press, UK, 17,726

CURRICULUM VITAE

I was born in Alula. I graduated from primary and secondary school in Adana. I completed my secondary school studies at Yıldırım Beyazıt İlköğretim Okulu. After that, I enrolled to the high school of Anafartalar Lisesi and graduated. I enrolled to the Physics Department in Çukurova University and I graduated in 2007. After my bachelor degree, I continued to study for my Master in High Energy Physics, at the Institute of Natural and Applied Sciences in Çukurova University where I am still enrolled.